Article:
Shaikhah, D, Barker, R orcid.org/0000-0002-5106-6929, Taleb, W orcid.org/0000-0003-2179-7963 et al. (4 more authors) (2022) Engineering of corrosion product-polymer hybrid layers for enhanced CO2 corrosion protection of carbon steel part one: Corrosion study and mechanical property investigation. Polymer, 242. 124614. ISSN 0032-3861

https://doi.org/10.1016/j.polymer.2022.124614

Engineering of Corrosion Product-Polymer Hybrid Layers for Enhanced CO_2 Corrosion Protection of Carbon Steel Part One: Corrosion Study and Mechanical Property Investigation

Dilshad Shaikhah[a*], Richard Barker[a], Wassim Taleb[a], Anastasija Lazareva[a], Maalek Mohamed-Said[b], Bruce Cowe[b] and Anne Neville[a]

[a]Institute of Functional Surfaces, School of Mechanical Engineering, University of Leeds, Leeds, United Kingdom, LS2 9JT

[b]TOTALEnergies, OneTech CSTJF, Avenue Larribau, F-64018 Pau, France

***Corresponding author: D.M.Shaikhah@leeds.ac.uk**

Abstract

The role of Poly(allylamine hydrochloride) (PAH) is investigated when applied *in-situ* during different stages of evolution of an iron carbonate ($FeCO_3$) corrosion product on X65 carbon steel surfaces in a CO_2 corrosion environment. We show that PAH adsorbs onto both $FeCO_3$ and the bare carbon steel surface, producing a $FeCO_3$-PAH hybrid structure that reduces both localised and general corrosion. The thickness and mechanical properties of naturally formed $FeCO_3$ and $FeCO_3$-PAH hybrid layers are characterised. The hybrid layers are shown to offer superior adhesion, as well as increased elasticity and delamination resistance compared with the naturally formed $FeCO_3$ layer.

Keywords

Carbon steel; CO_2 corrosion; iron carbonate; hybrid layer; corrosion inhibition; adhesion strength

1. Introduction

Due to low cost, mechanical durability and availability, carbon steel remains the most commonly used material for pipelines in down and upstream facilities within the oil and gas industry [1]. In hydrocarbon services, approximately half of carbon steel pipeline failures are attributed to either carbon dioxide (CO_2) or hydrogen sulfide (H_2S) corrosion [2]. To control corrosion on the internal wall of pipelines, the pH stabilisation technique has historically been utilised in several large wet gas pipelines. Although this approach benefits the formation of protective scales to inhibit corrosion, it is restricted to specific operations and exhibits limitations, i.e. blocking of pipelines can occur due to increased scaling tendency of other mineral deposits [3]. This can also potentially enhance pitting and localised corrosion in the long-term [4]. It is therefore prudent to explore alternative techniques that exploit the naturally formed scale and corrosion products. Ideally, these techniques should only influence the internal near surface of the pipeline and not the bulk solution.

The nature and characteristics of the corrosion product are heavily dependent upon the environmental and physical conditions in the pipeline. In some instances, corrosion products such as magnetite (Fe_3O_4), $FeCO_3$ (which develop predominantly in CO_2-containing environments) and iron sulphides (FeS) are capable of significantly inhibiting general corrosion [5–7], so it is arguably beneficial to maintain them. In relation to the $FeCO_3$ corrosion product, the protective properties of this layer with respect to general corrosion of carbon steel as well as in steel welded joints are well documented [5,8]. However, $FeCO_3$ protection efficiency can be constrained and local removal of this corrosion product via mechanical removal, chemical dissolution, or these combined processes is a precursor to localised corrosion. Additionally, the local heterogeneity or discontinuities in the layer developed during formation can initiate localised corrosion [9–11]. Therefore, the mechanical properties of $FeCO_3$ and their relationship with the tendency for localised corrosion to initiate/propagate are extremely important in relation to the lifespan of carbon steel pipelines. The ability to enhance $FeCO_3$ resilience to mechanical and chemical removal could be particularly useful in mitigating both corrosion and erosion processes.

In service, the internal pipeline will have potentially undergone corrosion prior to inhibitor application and may already have corrosion products present on the surface. Significantly, less work has been devoted to understanding corrosion inhibitor performance in environments where steel surfaces are partially or fully covered with corrosion products. However, the few studies that exist typically report that the addition of corrosion inhibitors in the presence of corrosion products on steel surface led to severe localised corrosion due to the inability of imidazoline type inhibitors to interact with such products or reach the steel substrate effectively [12,13]. Thus, increasing the inhibition efficiency towards localised corrosion seems requiring higher dosage for imidazoline type inhibitor. In academia and industry there is a distinct lack of development of corrosion inhibitors specifically tailored to function in the presence of corrosion products or interact with the corrosion products themselves, thus exploiting the natural formation of corrosion products for corrosion mitigation, particularly in the context of localised corrosion. Ultimately, the development of such inhibitors could produce combined corrosion product-inhibitor hybrid structures or exploit synergistic effects that provide superior protection.

In artificial biomineralisation systems, water soluble polymers have attracted significant attention in relation to the synthesis of hybrid materials, owing to their exceptional flexibility, high compatibility, cost, and strong adhesion affinity. Among polymers, synthetic anionic/cationic polymers are the most promised organic additives owing to their solubility in aqueous media and capability of interaction with metal carbonates during crystallisation [14,15]. An important example for cationic polymers is PAH polymer, a polymeric amine which has displayed significant morphological

modifications and physico-mechanical improvements in various applications [16–19]. PAH polymer, an eco-friendly and biodegradable polymer, is a water-soluble weak-base and a cationic polymer. It has a large number of amino groups that are present as a free amine or cationic ammonium salt like other amine group-containing polymers [20], as shown in Figure 1.

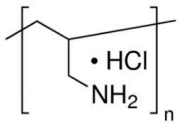

Figure 1. Chemical structure of PAH polymer, where n is the number of repeating units.

This study adopts a novel approach as an alternative to pH-stabilisation through the development and assessment of a biodegradable chemistry which interacts with both steel surface and $FeCO_3$ corrosion product, with a view to maintaining and enhancing the layer integrity. Specifically, this research exploits the naturally formed $FeCO_3$ corrosion product by developing a $FeCO_3$-PAH hybrid layer *in-situ*, consisting of $FeCO_3$ corrosion product (inorganic) and PAH polymer (organic). The corrosion measurements and corrosion inhibition characteristics of the newly formed $FeCO_3$-PAH hybrid layer are evaluated. The morphological analysis is subsequently investigated before characterisation of the coexistence of the hybrid layer. The influence on localised corrosion behaviour of the $FeCO_3$-PAH hybrid layer is also reported. Finally, the protective and physical properties (hardness, Young's modulus, delamination and shear stress) of $FeCO_3$-PAH hybrid layers are contrasted with a naturally and fully developed pure $FeCO_3$ layer.

2. Materials and methods

2.1.Materials

Based on its widespread use within the oil and gas industry, carbon steel (API 5L X65) was studied as the substrate choice material and formed the working electrode for the electrochemical experiments. The elemental composition of carbon steel is shown in Table 1, with the steel possessing a ferritic-pearlitic microstructure.

Table 1. Elemental composition in weight percentage (wt.%) of API 5L X65 carbon steel.

Elements	**Fe**	**Mn**	**Si**	**Mo**	**C**	**Cu**	**Cr**	**Ni**
Wt. %	97.808	1.270	0.180	0.170	0.120	0.120	0.110	0.070
Elements	**V**	**Nb**	**Al**	**P**	**Sn**	**S**	**Ti**	**B**
Wt. %	0.057	0.054	0.022	0.008	0.008	0.002	0.001	0.0005

The PAH polymer (average molecular weight: 100,000-150,000), was purchased from ThermoFisher Scientific and used without further purification. The carbon steel test specimens, (used as working electrodes for electrochemical studies), were cut into cuboids (15 mm x 15 mm x 5 mm). Electrical connections to working electrodes was achieved by soldering a copper wire to the reverse side, before embedding in a non-conductive resin, producing an exposed area of 2.25 cm^2 for corrosion measurements. The exposed test surface of each embedded specimen was subsequently wet ground up to 600 grit silicon carbide papers, followed by rinsing with deionised water and acetone before drying with nitrogen gas and placing in the aqueous test environment.

2.2.Experimental conditions

In order to investigate the interaction efficiency of PAH polymer with the carbon steel surface and its ability to inhibit the electrochemical reactions in a CO_2-containing aqueous environment, a series of *in-situ* electrochemical tests were performed. These tests were conducted using a conventional glass (or bubble) cell setup integrated with a three-electrode electrochemical cell and are described in detail in section 2.3 and Figure 2. A litre of brine solution was prepared with dissolving 35g sodium chloride (NaCl) (99% analytical grade - Sigma Aldrich) in 1 L deionised water for each experiment. The 1 L 3.5 wt.% NaCl brine solution was saturated with CO_2 overnight for at least 12 h by bubbling CO_2 gas through the solution continuously. Prior to the start of each experiment, the brine solution was heated to desired temperature (60°C) and the pH was adjusted to 6.7 via the addition of sodium bicarbonate ($NaHCO_3$). The test conditions are summarised in Table 2 and were selected as literature and previous experience of the researchers identified such conditions were highly conducive to the formation of a $FeCO_3$ layer on carbon steel within a 48 h test period.

Table 2. Operational conditions and polymer loadings used in the electrochemical experiments

Parameter	**Values**
Temperature	60°C
CO_2 partial pressure	~0.8 bar
Substrate material	Carbon Steel (API 5L X65 Steel)
Working solution	3.5 wt.% NaCl
pH	6.6 ± 0.20
PAH polymer concentration	1, 10 and 100 ppm
Time when PAH introduced to solution	2 h (for 1, 10 and 100 ppm), /24/34/44 h (for 100 ppm only)
Test duration	48 h

In experiments where PAH polymer was used, the chemical was pre-dissolved in the same fluid as the corrosion experiment and injected directly into the test solution. For instance, to have 1 ppm PAH in the 1 L brine test solution of the experiment, 1 mg of PAH polymer was dissolved in the same fluid as the corrosion experiment and added into the 1 L brine solution using a micro-pipette.

Initially, the influence of concentration (1, 10 and 100 ppm) was assessed with a fixed pre-corrosion period of 2 h. As the concentration of most common polymeric corrosion inhibitors for the oil and gas industry is approximately between 10-1000 ppm [21], the subsequent tests involved examination of the effect of pre-corrosion time (and hence, extent of $FeCO_3$ evolution/formation) on PAH performance, with the chemical concentration maintained at 100 ppm. This would also offer a greater extent of polymer to interact with steel surface and corrosion product layer, facilitating morphological and mechanical property analysis.

2.3. Electrochemical methods

Electrochemical measurements were recorded using a conventional three-electrode cell connected to an ACM Gill 12 potentiostat. The three-electrode cell consisted of a working electrode, as described in section 2.1, and a combined Ag/AgCl reference (4M KCl)/platinum electrode which acted as the reference and counter electrode, respectively (Figure 2).

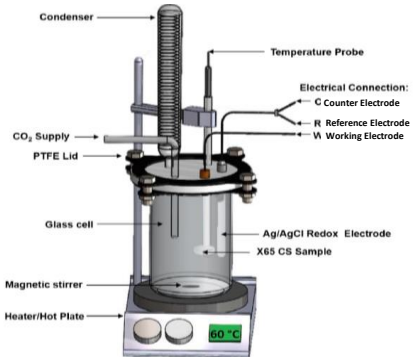

Figure 2. Three-electrode glass (bubble) cell used for electrochemical experiments.

Direct current electrochemical methods (namely, linear polarisation resistance (LPR) and potentiodynamic polarisation measurements) were used to determine the transient response in corrosion rate in each experiment. LPR measurements were performed every 15 minutes by polarising the working electrode ± 15 mV vs open circuit potential (OCP) at a scan rate of 10 mV/min. In each electrochemical measurement, the polarisation resistance (R_p in $\Omega.cm^2$) was determined from the slope of potential vs current plot [22]. This relationship is shown in Equation (1).

$$\frac{\Delta E}{\Delta I} = R_p \qquad \text{Eq. 1}$$

The polarisation resistance is related to the corrosion current density, i_{corr} through the expression in Equation (2).

$$i_{corr} = \frac{\beta_a \beta_c}{2.303\ R_p\ (\beta_a + \beta_c)} \qquad \text{Eq. 2}$$

where i_{corr} is corrosion current density (mA/cm^2) and β_a and β_c are the measured anodic and cathodic Tafel slopes, respectively, (both assumed as ± 120 mV).

From calculated values of i_{corr}, the rate of corrosion can be determined in desired unit (mm/yr) utilising Faraday's law (Equation (3)):

$$V_c = K\ \frac{i_{corr} M_{Fe}}{nF\rho} \qquad \text{Eq. 3}$$

where *K* is a conversion factor to obtain corrosion rate (V_c) in units of mm/year (K = 3.16×10^5), M_{Fe} is the molar mass of iron (55.8 g), *n* is the number of electrons freed in the corrosion reaction (2 electrons – Fe^{2+}), F is the Faraday constant (96, 485 C/mol) and ρ is the density of steel (7.87 g/cm^3) [23].

Upon the completion of electrochemical tests, the steel specimens were rinsed with deionised water, acetone and dried gently with nitrogen gas before storing in a desiccator under vacuum for *ex-situ* analysis.

Potentiodynamic polarisation measurements were performed at strategic times (2, 3 and 48 h corrosion time), where significant modification on steel surface occurred. It should be stressed that each test was carried out in completely separate cells. The scans for $FeCO_3$ were collected at 2 h and end of the immersion test (48 h). After addition of PAH polymer at 2 h of exposure time and resting steel surface for an hour, the polarisation scan (3 h) was conducted. The scan at 48 h for $FeCO_3$-PAH polymer was taken when PAH polymer was introduced at 24 h pre-corrosion to explore the

interaction of PAH polymer with pre-grown $FeCO_3$ layer on the steel surface. Anodic and cathodic Tafel polarisation was conducted by polarising up to ± 500 mV vs OCP at a scan rate 15 mV/min. Each branch of the Tafel plot (anodic and cathodic) were collected on separate test specimens in separate test vessels. Equation (4) was used to calculate the inhibition efficiency (IE%) where i_0 and i_{corr} are the corrosion current density values without and with inhibitor, respectively:

$$IE\% = \frac{i_0 - i_{corr}}{i_0} x\ 100 \qquad \text{Eq. 4}$$

In addition, for the electrochemical impedance spectroscopy (EIS) measurements, the DC potential was 0 mv vs OCP but the AC amplitude was 10mV (rms) with a frequency range of 5 mHz to 10 kHz with ten points per decade. The measurements were taken at 4, 24 and 48 h in the absence and presence of PAH polymer tests.

Commented [DS[1]: The amendment for the first comment of Reviewer one

2.4. Surface and chemical analysis methods

To assess the coverage and topography of the $FeCO_3$ and $FeCO_3$-PAH hybrid layers, Scanning Electron Microscopy (SEM) using a Carl Zeiss EVO MA15 was conducted on carbon steel specimens at the end of the experiment (48 h). Energy Dispersive X-ray spectroscopy (EDX) using the same SEM enabled elemental mapping of desired regions on steel surface. Both the imaging and EDX analysis were performed at an acceleration voltage of 20 kV and working distance of 8-10 mm.

A FEI NOVA200 dual beam focused ion beam-SEM (FIB-SEM) was utilised to analyse the thickness of $FeCO_3$ crystal layer and adsorbed PAH polymer layer on both the $FeCO_3$ and bare steel surface. Test specimens were initially coated with platinum in selected areas within the FIB-SEM to protect the surface while trenches were milled using a Gallium ion beam in preparation for cross-section analysis via SEM and EDX. A voltage and current range of 5-30 kV and 0.1-5 nA were used for the milling process, after which, the sample stage was tilted for microscopy and spectroscopic analysis of the layer cross-section.

Fourier Transform Infra-Red Attenuated Total Reflectance (FTIR-ATR) measurements of $FeCO_3$ and $FeCO_3$-PAH hybrid layers on carbon steel test specimen surfaces were performed using a Perkin Elmer spectra 100. For each set of spectra acquired the background signal was collected which was subsequently subtracted from the spectra collected from each test specimen surface. The spectra were collected between a wavelength range of 4000-650 cm^{-1}. The obtained spectra were interpreted using the hand book of IR spectra for both organic and inorganic compounds [24].

2.5. Surface profilometry

The extent of localised corrosion on the X65 carbon steel surface was evaluated utilising a 3D surface profilometer Bruker NPFlex™. Before analysis, the post-test specimens were prepared by cleaning the surface using Clarke's solution in accordance with ASTM Standard G 1-03 [25]. For each experimental condition, two square specimens (15 x 15 mm^2) were scanned with a total area of 196 mm^2 (14 x 14 mm^2) on each specimen. The raw data was analysed in Vision64 software package by applying carefully selected thresholds with distinct pit depths, diameters and areas being quantified, in alignment with previous work [12,26].

2.6. Mechanical property analysis

2.6.1. Hardness and Young's modulus

Nanoindentation tests were implemented employing the Nano Test (Micro Materials Limited, UK), with a Berkovich diamond indenter. For reliant analysis, 100 loading/unloading curves were

computed in each experiment to find the average results. All experiments were carried out at a constant loading and unloading rate equal to 0.2 mN/s and to a maximum load of 1 mN (controlled maximum load). The hold time at maximum load was 20 s, and thermal drift correction was set at 60 s of holding period at 80% unloading. The unloading curves were used to derive the hardness and modulus values by analytical technique developed by Oliver and Pharr [27].

2.6.2. Scratch test and shear stress

The scratch test was performed, via a TriboTechnic Millenium 200 scratch tester, progressively using a load (0-50 N) over a length of 10 mm with a scratching speed of 10 mm/min. The indenter was a Rockwell C geometry and the protocol was followed according to ASTM G 171-03 [28]. Table 3 shows the scratch test parameters used to characterise the noticeable damage, failure mode and critical load for $FeCO_3$ and $FeCO_3$-PAH hybrid layers.

Table 3. Conditions for progressive load scratch test

Parameter	**Values**
Indenter material	Diamond
Indenter geometry	Rockwell C (120° sphero-conical)
Indenter tip radius (μm)	200
Type of Load	Progressive
Progressive Load (N)	0 – 50
Scratch test length (mm)	10
Scratching Speed (mm/min)	10

The different loads at each collected SEM image of the wear scar were calculated by measuring the length of the scratch from the starting point to region of interested and correlating this with the output graphs (load vs length) obtained from TriboTechnic Millenium 200 scratch tester. From their study, Oliver and Pharr [27] stated that the adhesive properties of a layer can be estimated if the mode of failure of the layer is determined. Prieto et al. [29], successfully corroborated this methodology for pure $FeCO_3$ layer deposited onto carbon steel and from there analysed the shear stresses required to generate small damage, partial removal and full delamination of pure $FeCO_3$ layer. Additionally, it was indicated that the mode of failure for $FeCO_3$ on carbon steel is expected to be buckling mode. From the buckling mode area, the critical load can be determined, and it is this parameter which is paramount in the determination of shear stress. The buckling mode and stages of removal of pure $FeCO_3$ layer are demonstrated schematically in Figure 3. Here, we followed the same principles, using a progressive load (1 to 50 N) to analyse the adherence strength of the $FeCO_3$-PAH hybrid layer in comparison with the pure $FeCO_3$ layer generated within this study.

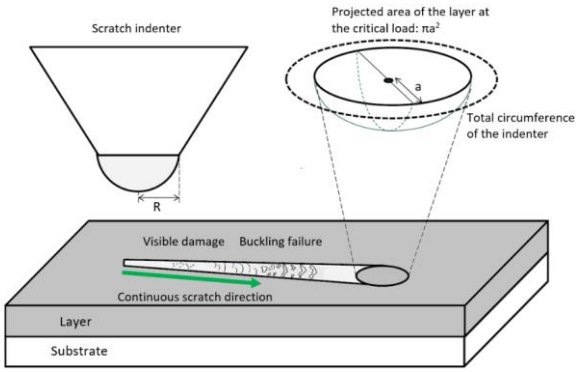

Figure 3. Schematic illustration of scratch test principle used in this study to delaminate the PAH-$FeCO_3$ or $FeCO_3$ layer (grey) on a carbon steel substrate (white), adapted from reference [29]. The parameter "R" is the radius of indenter cone and "a" is the radius of the projected area after scratch. These parameters are required to determine shear stresses.

After finding critical loads, Olivier and Bull [27,30] proposed the theory and methodology for determination of the critical shear stress for adhesive films. In this study, the same model was applied to detect the shear stresses, which caused minimal damage, partial removal and full removal of $FeCO_3$ and hybrid layers. Essentially, the shear stresses were calculated using Equation (5) which is dependent on the load and radius of the projected area measured in the desired detachment area:

$$\tau = \frac{L_c}{\pi a \sqrt{R^2 - a^2}} \quad \text{Eq. 5}$$

where τ is the shear stress (Pa); L_c is critical load (N); R is the indenter radius (m) and a is the radius of the projected area (m).

3. Results and Discussion

3.1. Corrosion evolution

3.1.1. PAH polymer concentration optimisation

To determine the influence of PAH polymer concentration in terms of inhibition efficiency, three different concentrations were selected (1 ppm, 10 ppm and 100 ppm) in alignment with the studies of polymeric corrosion inhibitors in hydrocarbon production industry [21]. Figure 4(a) shows the corrosion rate response of carbon steel in an uninhibited system as a function of time over two days, whilst Figure(b) shows experiments where the PAH polymer was injected into the system after 2 h of pre-corrosion at the three aforementioned concentrations (1, 10 and 100 ppm). The uninhibited experiment (Figure 4(a)) illustrates that the corrosion rate drops to around 0.1 millimetre/year (mm/yr) after 40 h of exposure. This effect is attributed to the formation of pure $FeCO_3$ layer on the steel surface (as reported in previous studies [5,26]), which reduces the dissolution of the underlying carbon steel by acting as a diffusion barrier and/or blocking active sites on the steel surface.

When the PAH polymer was introduced into the corrosive environment after 2 h pre-corrosion (Figure 4(b)), regardless of the concentration (1, 10, or 100 ppm) the corrosion rates dropped rapidly from ~1.5 mm/yr (within 10 minutes) by ~1 mm/yr and continued to decrease to corrosion rates of ~0.1 mm/yr after 48 h. Despite an order of magnitude change in concentration of PAH polymer, very similar efficiency was achieved, indicating that PAH is effective in reducing corrosion at concentrations of 1 ppm. In comparison with other organic corrosion inhibitors available in literature

[31], this polymer immediately after injection decreased the corrosion rate to the level of residual corrosion rate regarded as acceptable for field application (0.1 mm/yr); this is discussed in detail in section 3.1.3.

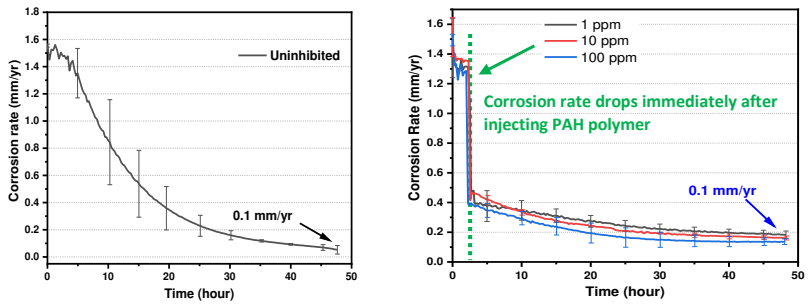

(a) (b)

Figure 4. Corrosion rate of carbon steel vs time in (a) uninhibited experiment and (b) for different concentrations of PAH polymer (1, 10 and 100 ppm) introduced after 2 h of pre-corrosion. Test conditions are pH=6.6, 60°C, 3.5 wt.% NaCl, pCO_2=0.8 bar.

The selected concentration for PAH polymer in various applications for mechanical property enhancement is around 1000 ppm [18,32] whilst polymeric corrosion inhibitor dose rate in the oil and gas industry are between 10-1000 ppm [21]. Thus 100 ppm was selected as a desired concentration for surface analysis and mechanical property investigation.

3.1.2. Effect of PAH polymer introduction at different stages of $FeCO_3$ surface growth

To understand the impact of PAH polymer on the corrosion inhibition mechanism and the interaction with $FeCO_3$ during the crystal growth process to form a robust $FeCO_3$-PAH hybrid layer, the PAH polymer was injected at various stages of $FeCO_3$ surface growth on the carbon steel in the CO_2 saturated media. The corrosion rate and the OCP measurements for experiments using 100 ppm PAH polymer are shown in Figure 5; the data are plotted as a function of time. The corrosion rate results in Figure 5(a) indicates that, in the absence of PAH polymer, the corrosion rate shows a steady decline during the period 5-48 h. Figure 5(b) shows that the corrosion rate dropped rapidly (within 10-15 mins) when the PAH polymer was injected after 24, 34 and 44 h of pre-corrosion. As PAH polymer reduces uniform corrosion, the potential release and transference of Fe^{2+} from the steel surface is restricted. Consequently, the extent of precipitation/crystal growth of $FeCO_3$ is limited after addition of PAH.

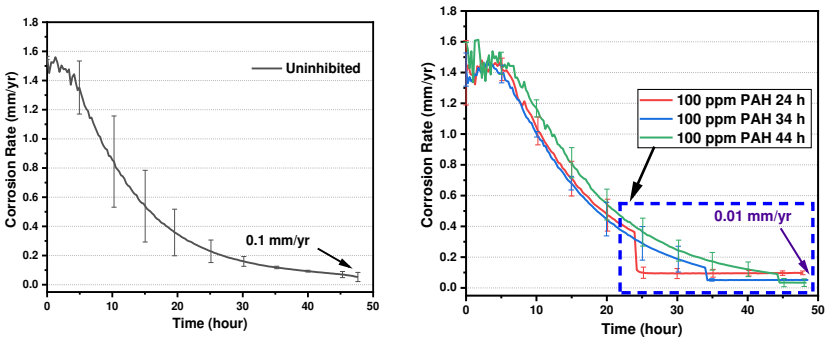

(a) (b)

Figure 5. General corrosion rates against time when 100 ppm PAH polymer was introduced at different h of pre-corrosion; (a) uninhibited experiment (b) inhibited tests for 24, 34 and 44 h of pre-corrosion.

3.1.3. $FeCO_3$ – PAH hybrid layer performance

Figure 6 shows the generalised inhibition efficiencies reached at the end of each experiment (based on an end-point calculation) as a function of the time at which PAH polymer is introduced into the test solution. Utilising Equation (6), the end-point inhibitor efficiency was calculated from the corrosion rate before the inhibitor was injected and the final corrosion rate after 48 h of exposure:

$$E_{Endpoint}(\%) = \left[1 - \left(\frac{CR_{\,Inhibited}}{CR_{Uninhibited}}\right)\right] \times 100 \qquad \text{Eq. 6}$$

Where $CR_{\,Inhibited}$ is the inhibited corrosion rate at the end of the test (mm/yr) and $CR_{Uninhibited}$ is the uninhibited corrosion rate before inhibitor injection (mm/yr).

The results in Figure 6(a) indicate that PAH polymer is an efficient inhibitor in any pre-corrosion period introduced. More interestingly, with exception of the uninhibited experiment, the graph clearly illustrates that introducing PAH polymer later into the brine solution later (24, 34 and 44 h) in the experiment resulted in offering higher corrosion protection (increasing from 88% to 98%). Beyond 24 h of pre-corrosion/$FeCO_3$ layer evolution, the synergistic effect between the $FeCO_3$ and PAH layer produces a layer which is more efficient at reducing general corrosion than that of pure $FeCO_3$ layer.

To explore further the PAH's positive synergistic effect, the individual inhibition efficiency of PAH polymer, as a corrosion inhibitor, and corrosion product $FeCO_3$ were calculated for each experiment, as shown in Figure 6(b). For the uninhibited experiment, the pure $FeCO_3$ layer produced 91% protection efficiency, while PAH polymer alone inhibited 88% of corrosion when it was introduced at 2 h of pre-corrosion. Moreover, introducing PAH polymer into the brine solution later (24 h) added 21% protection efficiency to what was already provided by $FeCO_3$ layer (73%) resulting in 94% inhibition. Similar increment in inhibition efficiency were achieved when PAH polymer was injected at 34 and 44 h of pre-corrosion, but with a lower magnitude of additional efficiency (7-8%), as there was a higher pre-corrosion time for evolution of the $FeCO_3$ layer and hence, a greater initial contribution to efficiency. These results illustrate that PAH polymer interacts/cooperates with the

already formed $FeCO_3$ layer on the steel surface, resulting in a more efficient $FeCO_3$-PAH hybrid layer. Such observations are unusual, as numerous studies with more 'conventional' CO_2 corrosion inhibitors report pre-corrosion and corrosion product formation as having a detrimental effect on the inhibitor performance [12,13,33]. The reason for a higher corrosion efficiency of $FeCO_3$-PAH hybrid layer being observed when the pre-corrosion period is extended could be attributed to the requirement of a well-established (crystallised) $FeCO_3$ layer and the Fe_3C surface being more accessible for interaction with PAH polymer in a longer period prior to injecting PAH polymer. The optimisation of pre-corrosion period to create a more resilient $FeCO_3$-PAH hybrid layer with optimum inhibition efficiency as well as robustness in mechanical properties should be investigated further.

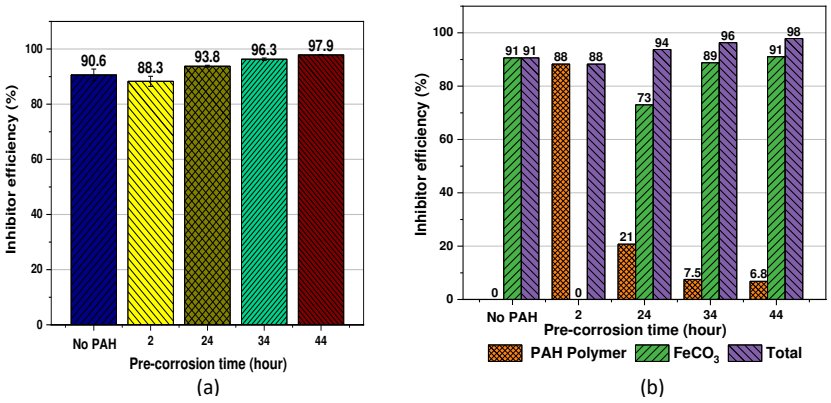

Figure 6. (a) Total uniform corrosion inhibitor efficiency and (b) segregated uniform corrosion inhibitor efficiency after 48 h as a function of time at which PAH polymer was introduced to the brine solution i.e. after specified pre-corrosion/$FeCO_3$ layer formation times.

3.1.4. Potentiodynamic polarisation – PAH adsorption mechanism

The corrosion rate vs time and current–potential relationships (cathodic and anodic) for 100 ppm PAH polymer addition after 2 and 24 h are shown in Figure 7, which consists of four potentiodynamic polarisation plots each taken independently in separate experiments at different points in the overall test. First scan was collected after 2 h of pre-corrosion before PAH addition, while the second plot was taken after 48 h in the absence of PAH polymer (in a separate experiment). Immediately after 100 ppm PAH polymer addition at 2 h pre-corrosion in a separate setup, the third plot was obtained (once OCP reached a quasi-steady state value around 3 h pre-corrosion) and the final plot was achieved at the end of the 48 h separate measurement when PAH was introduced at 24 h pre-corrosion. The collective measurements provide an insight into the inhibition mechanism as well as its time dependency.

In the absence of PAH polymer (first and second plots in Figure 7), the formation of $FeCO_3$ layer modifies the steel surface corrosion behaviour, providing higher protection as the current density shifts to a lower value while OCP increases slightly. Immediately after the addition of PAH polymer (third scan), the OCP rises by 30 mV and the currents associated with the anodic and cathodic reactions are reduced by approximately a factor of three. Consistent with previous work [34,35], this

behaviour is indicative of PAH polymer behaving as a mixed-type CI, with both the anodic and cathodic reactions being similarly impeded [36]. Furthermore, the gradients of the anodic and cathodic reactions are typical of geometrical blocking effect through establishing a protective hydrophobic film on the steel surface, which blocks the active anodic/cathodic sites of carbon steel [37]. It can be observed from the plot number 4 in Figure 7 that the addition of PAH polymer at 24 h pre-corrosion exhibits maximum shifts in current density and OCP. This suggests that introducing PAH polymer at the correct point creates a hybrid layer that is more effective than that of pure $FeCO_3$ layer.

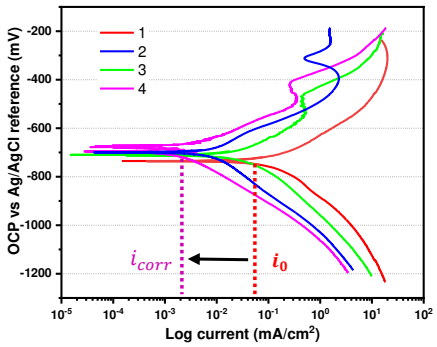

Figure 7. Potentiodynamic polarisations at different times during a 48 h experiment in the absence of PAH polymer (scan 1: at 2 h of immersion and scan 2: at the end of 48 h immersion) and presence of 100 ppm PAH polymer (scan 3: at 3 h when PAH was added an hour before and scan 4: at the end of 48 h immersion test where PAH was introduced at 24 h pre-corrosion). Test conditions are pH=6.6, 60°C, 3.5 wt.% NaCl, pCO_2=0.8 bar, 48 h. Note: Each potentiodynamic scan was taken from completely independent experiments.

Electrochemical corrosion parameters such as corrosion potential (OCP), cathodic and anodic Tafel slops (β_a, β_c) and corrosion current density (I_{corr}), obtained by extrapolation of Tafel lines, are listed in Table 4. Administrating PAH polymer at 2 h pre-corrosion decreased corrosion current density and increased protection efficiency suggesting an immediate interaction of PAH polymer with steel surface. Although formation of $FeCO_3$ after 48 h measurement, in the absence of PAH polymer, shifts E_{corr} value to a higher value and corrosion current density to a lower value, the $FeCO_3$-PAH hybrid layer shows a greater shift in the values of E_{corr} and I_{corr} providing greater corrosion protection to steel surface. The values of β_a and β_c (Table 4) are impeded in a similar manner with introducing PAH polymer to the system, indicating that PAH could control both the anodic and cathodic corrosion reactions. This also implies that the PAH polymer is able to co-operate with the $FeCO_3$ layer available on the steel surface in blocking corrosion active sites. Most importantly, the PAH polymer shows greater inhibition efficiency in the presence of $FeCO_3$, implying the synergistic impact of PAH polymer with $FeCO_3$ in creation of a more protective layer compared with the pure $FeCO_3$ layer.

Table 4. Polarisation parameters for carbon steel specimens in in the absence and presence of 100 ppm PAH polymer introduced at 2 & 24 h pre-corrosion (pH=6.6, 60°C, 3.5 wt.% NaCl, pCO_2=0.8 bar).

Time (hour)	E_{corr} (mV)	β_a (mV)	β_c (mV)	i_{corr} (mA/cm^2)	CR (mm/yr)	I%
2 h $FeCO_3$	-740	116	160	0.1410	1.64	-
48 h $FeCO_3$	-697	113	141	0.0099	0.12	92.97
3 h $FeCO_3$ – PAH polymer	-708	116	148	0.0276	0.31	80.87
48 h $FeCO_3$ – PAH polymer	-685	87	136	0.0026	0.03	98.11

3.1.5. Electrochemical impedance spectroscopy

Aforementioned corrosion rate measurements illustrate the evolution of the dissolution of the steel surface introducing PAH polymer at different times in a CO_2 environment. To provide further insight into the corrosion mechanisms occurring at the interface, electrochemical impedance spectroscopy measurements were utilised to understand the influence of PAH polymer on the corrosion behaviour of X65 in the CO_2 containing medium. Specimens were subjected to corrosion for 48 hours in the absence and presence of 100 ppm PAH polymer. Three critical times (4 h, 24 h and 48 h), where the polarisation resistance had suddenly changed, were selected to investigate. Figure 8 displays the Nyquist plots of the electrochemical impedance spectra at 4 h, 24 h and 48 h for specimens obtained in the presence and absence of PAH polymer for the two-day immersion tests.

In the absence of PAH polymer, for the first 4 h of steel exposure, two time constants were identified; a capacitive semicircle in the high–medium frequencies range, and an inductive loop in the low frequency range, as per Figure 8(a-1). The capacitive semicircle ascribes the active state of the interface when steel was exposed to the CO_2-saturated solution. The evolution of the impedance signature characteristic of inductive behaviour observed at low frequency has been attributed to the adsorption of an intermediate product on the steel surface [38].

Additionally, the inductive behaviour disappears with respect to corrosion time and the amplitude of the loop, Figure 8(a2-3), increases indicating that the charge-transfer process slows down [39]. The critical point appears approximately at 24 h of corrosion. The impedance characteristic of this electrode surface is a capacitive reactance arc. According to equivalent electrical circuits for 24 and 48 h corrosion time illustrated in Figure 9(b), there is only one layer on carbon steel surface which is the CO_2 corrosion product layer ($FeCO_3$) consisting of C_{FeCO3} and R_{FeCO3} in addition to the existing structure that consists of electric double layer capacitance (C_t) and transfer resistance (R_t). These parameters of the equivalent electrical circuit are listed in Table 5, where the resistances and capacitances are illustrated in Figure 10(a). The resistance of $FeCO_3$ layer (R_{FeCO3}) increases significantly with time from 24 to 48 h as the $FeCO_3$ grows on the steel surface, indicating a denser $FeCO_3$ layer formation that influences the active sites of the steel [38]. The C_t, C_{FeCO3}, R_t and R_{FeCO3} magnitudes in Table 5 corroborate the corrosion rate reduction in time between 24 and 48 h of exposure.

Figure 8(b-1 to b-3) depict Nyquist plots where 100 ppm PAH polymer is introduced at 2 h and 20 h pre-corrosion. In comparison with its absence, PAH polymer at 4 h corrosion time increases the amplitude of the loop, signifying the strong interaction of polymer with the steel surface. More interestingly, the amplitude of the loops continues to increase with exposure time (24 and 48 h) suggesting a positive synergistic influence of PAH polymer cooperating with steel surface as well as $FeCO_3$ layer to reduce general corrosion, which is in consistent with achieved LPR corrosion measurements in Figure 5(b) and surface analysis images discussed later.

Moreover, the equivalent electrical circuits for $FeCO_3$ layer and $FeCO_3$-PAH hybrid layer are depicted in Figure 9. Formation of $FeCO_3$ layer in the absence of PAH polymer on steel surface after 48 h showed an additional time constant, as per Figure 9(b), to the existed time constant for double layer initially (Figure 9(a)). In the beginning of the test when PAH polymer was present at 4 h exposure time, the surface reveals the existence of an extra layer on the steel surface composed of C_{PAH} and R_{PAH} adding to the existed double layer constant element (C_t and R_t), as per Figure 9(c). At longer corrosion times (24 h and 48 h), the equivalent electrical circuits depicted in Figure 9(d) suggest the existence of one layer on steel surface, which implies a joint structure consisting of $FeCO_3$ layer and PAH polymer, in additional to the electrical double layer. The values of equivalent electrical circuit are presented in Table 5 and 6, while the resistances and capacitances are revealed in Figure 10. As expected, the layers show higher values in resistance and lower values in capacitance with exposure time. From Table 6 and Figure 10(b), it can be noted that the resistance of PAH layer alone at 4 h corrosion time is much lower than of the resistance of the $FeCO_3$-PAH hybrid layer measured at 24 and 48 h exposure time implying the addition of resistance by PAH to the resistance of available and growing $FeCO_3$ layer. When compared with resistivity of pure $FeCO_3$ layer in Figure 10(a), the $FeCO_3$-PAH hybrid layer shows higher resistivity (Figure 10(b)) indicating an enhancement in corrosion protection corroborating with experimental results seen in Figure 6 and Figure 7 generated using the LPR and potentiodynamic polarisation approaches.

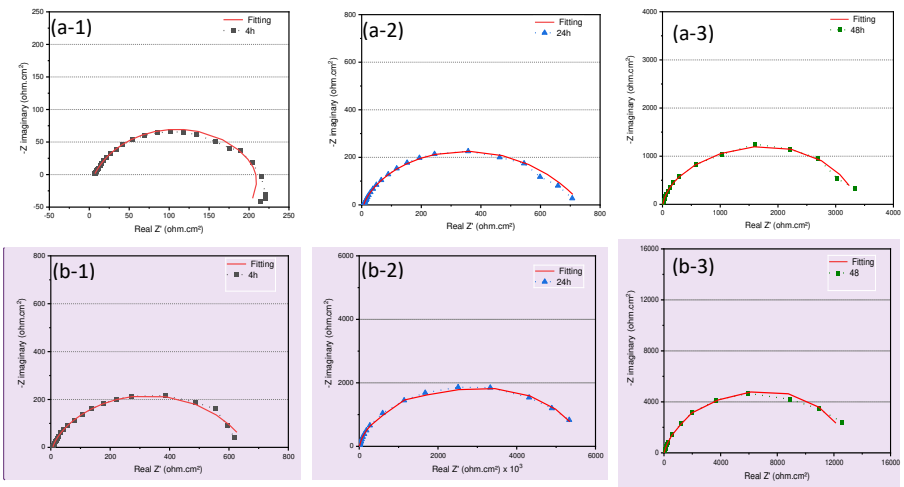

Figure 8. Nyquist plots of impedance diagrams for samples obtained for steel surface with $FeCO_3$ layer (a-1 to a-3) and for steel surface with $FeCO_3$ – PAH polymer layer (b-1 to b-3). (pH=6.6, 60°C, 3.5 wt.% NaCl, pCO_2=0.8 bar).

Commented [DS2]: The X and Y axes of graphs are amended, as per comment number two of Reviewer Two

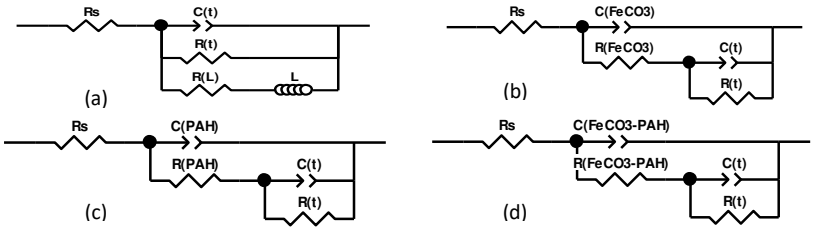

Figure 9. Equivalent electrical circuit model for steel surface with $FeCO_3$ layer: at 4 h (a) and for 24 to 48 h (b) of exposure time, whereas the model for steel surface with $FeCO_3$ – PAH polymer layer: at 4 h (c) and 24 to 48 h (d). (pH=6.6, 60°C, 3.5 wt.% NaCl, pCO_2=0.8 bar).

Table 5. Parameters of the equivalent electrical circuits at different corrosion times (4, 24 and 48 h) for $FeCO_3$ layer on steel surface. (pH=6.6, 60°C, 3.5 wt.% NaCl, pCO_2=0.8 bar)

Time (h)	R_s (Ω cm^2)	R_t (Ω cm^2)	R_{FeCO3} (Ω cm^2)	C_t (μF cm^{-2})×10^{-4}	C_{FeCO3} (μF cm^{-2})×10^{-4}	n_t	n_{FeCO3}
4	6.514	207.1	--	6.62	--	0.756	--
24	7.038	726.9	8.9	4.06	2.16	0.574	0.919
48	7.265	1605	1874	3.01	1.99	0.757	0.903

Table 6. Parameters of the equivalent electrical circuits at different corrosion times (4, 24 and 48 h) $FeCO_3$ – PAH polymer layer on steel surface. (pH=6.6, 60°C, 3.5 wt.% NaCl, pCO_2=0.8 bar)

Time (h)	R_s (Ω cm^2)	R_t (Ω cm^2)	R_{PAH} (Ω cm^2)	$R_{FeCO3-PAH}$ (Ω cm^2)	C_t (μF cm^{-2}) ×10^{-4}	C_{PAH} (μF cm^{-2}) ×10^{-4}	$C_{FeCO3-PAH}$ (μF cm^{-2}) ×10^{-4}	n_t	n_{PAH}	$n_{FeCO3-PAH}$
4	7.11	489.4	170	--	4.42	1.89	--	0.615	0.884	--
24	7.28	3243	--	2687	1.51	--	1.86	0.705	--	0.904
48	7.68	3456	--	9712	1.43	--	1.82	0.963	--	0.851

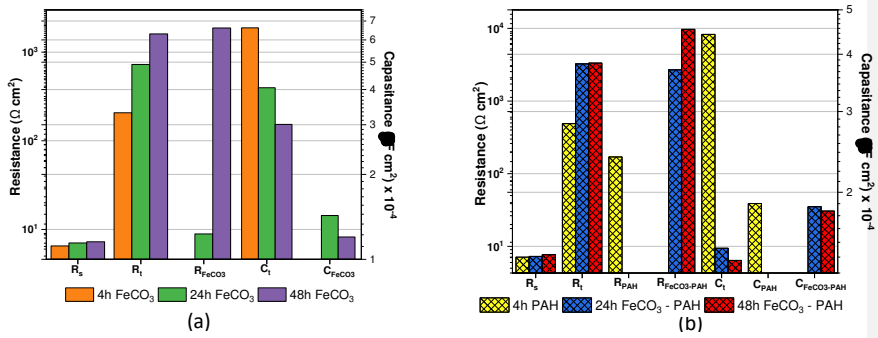

Figure 10. Resistance and capacitance of fitted equivalent electrical circuits at different corrosion times (4, 24 and 48 h) for $FeCO_3$ layer (a) and $FeCO_3$ – PAH hybrid layer (b) on the steel surface. (pH=6.6, 60°C, 3.5 wt.% NaCl, pCO_2=0.8 bar).

3.2. Surface analysis of $FeCO_3$ and $FeCO_3$-PAH layers

Figure 11 depicts the morphology of the corrosion product formed on carbon steel in the uninhibited environment after 48 h (Figure 11(a1-a3)) in conjunction with the hybrid $FeCO_3$-PAH form after 48 h when PAH is introduced after 24 h (Figure 11 (b1-b4)) and 34 h (Figure 11(c1-c3)) pre-corrosion time. As shown in Figure 11(a1-a3), the steel surface was well covered and packed with $FeCO_3$ crystals after 48 h of corrosion in the uninhibited environment. In both experiments where PAH was administered in the presence of a partially formed $FeCO_3$ layer, examination of the steel surface (Figure 12(b - c)) revealed that the polymer was adsorbed onto both the bare surface and $FeCO_3$ itself. The footprint of $FeCO_3$ crystals could be clearly observed under the transparent PAH polymer layer (i.e. Figure 12(b3)). It is suggested that the amine and ammonium groups inside PAH polymer are capable of complexation with iron atoms of bare steel as well as $FeCO_3$ crystal layer [40,41]. From there, the mechanism of adsorption on both sides uniformly are initiated. These observations of complexation and adsorption mechanism are an ongoing investigation and not included in the present study.

The micrographs also show that the extent of adsorption of the polymer is such that there is a noticeable coverage across both the $FeCO_3$ crystals and bare steel surface, hence this layer appears to be visibly thicker than those associated with other, more common organic corrosion inhibitors for CO_2 systems, which function through the creation of an adsorbed mono-layer or bi-layer. For instance, using Atomic Force Microscopy a study showed that the thickness of imidazoline inhibitor layer adsorbed bi-layer onto carbon steel is only a few nanometers (4 nm) [42]. However, the PAH polymer layer is able to cover and/or fill the voids/crevices between crystals, essentially interconnecting them to create a hybrid structure suggesting a stable interaction. It is assumed that the presence of cracks in the PAH layer are an artifact of the removal process and are formed during the post experiment drying process, as the polymer exhibits a gel-like state within the aqueuous phase. This state is due to the presence of higher content hydrophobic part (backbone and allyl group) in its chemical structure comparable with water soluble part (amine and especially ammonium groups), as per Figure 1.

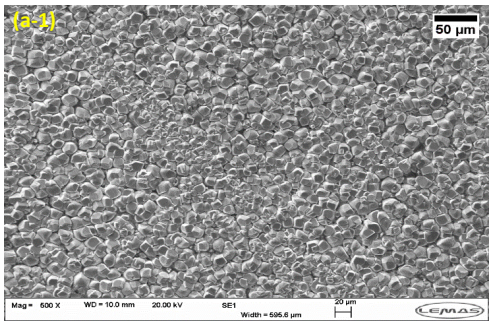

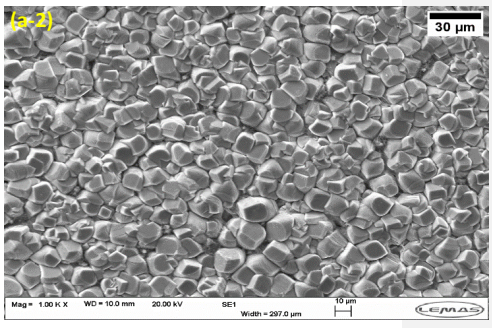

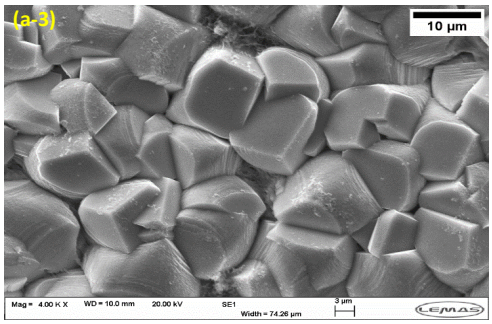
(a-3)
10 μm

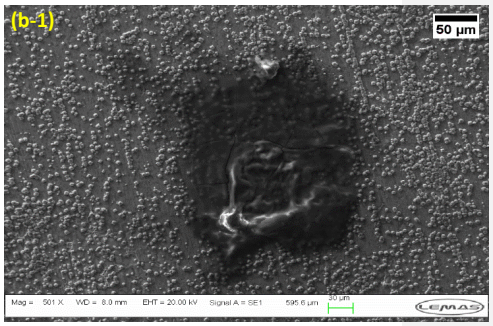
(b-1)
50 μm

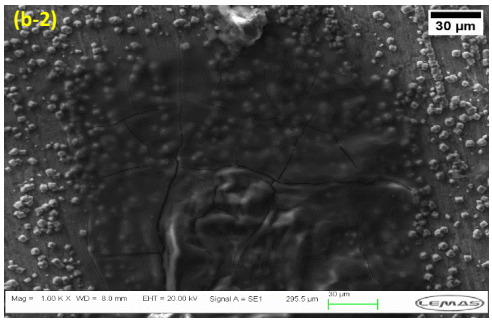
(b-2)
30 μm

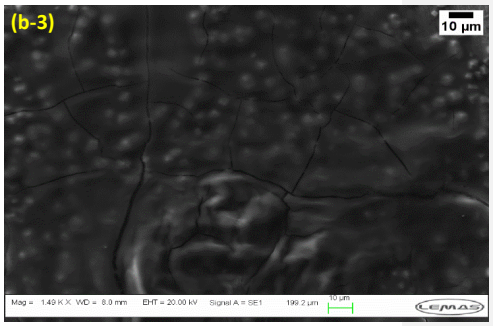
(b-3)
10 μm

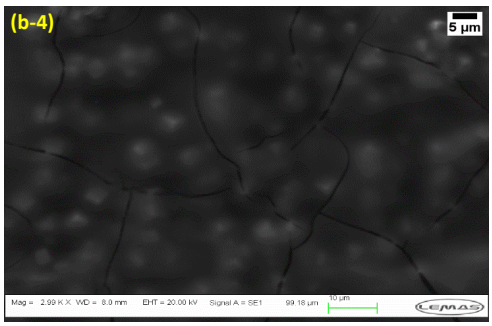
(b-4)
5 μm

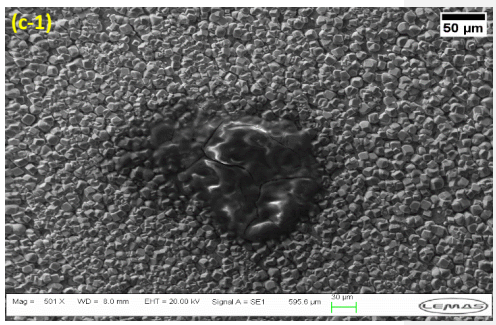
(c-1)
50 μm

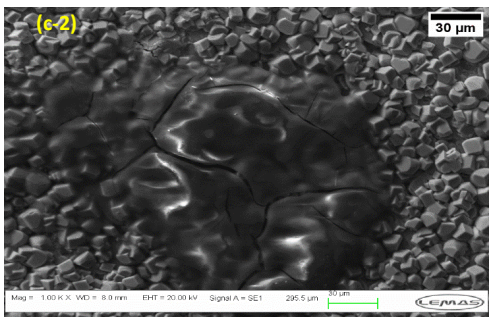
(c-2)
30 μm

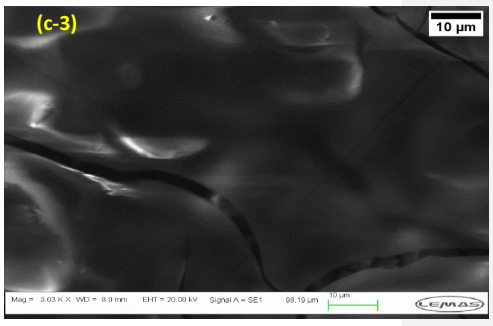
(c-3)
10 μm

Figure 11. SEM micrographs of the surface of carbon steel test specimen immersed for two days in (a) uninhibited system, (b) the system containing 100 ppm of PAH polymer introduced at 24 h and (c) the system containing 100 ppm of PAH polymer introduced at 34 h (pH=6.6, 60°C, 3.5 wt.% NaCl, pCO_2=0.8 bar).

3.3. Focused ion beam-scanning electron microscopy (FIB-SEM) investigation

Focused ion beam-scanning electron microscopy (FIB-SEM) was used to evaluate the thickness and elemental composition of deposited layers, as well as insight into the hybrid film growth process. Figure 12 shows the FIB-SEM micrographs of carbon steel specimens exposed to corrosion for 48 h. Figure 12(a1-a3) represent the uninhibited system, whilst Figure 12(b1-b5) are for the inhibited PAH system where the inhibitor is introduced after 2 h and the experiment is allowed to run for a further 46 h. A distinct PAH polymer layer over an individual crystal exposed to the inhibited environment is clearly visible from the FIB micrographs in Figure 12(b2, b3). The PAH polymer underneath the deposited platinum layer, used to protect the surface structure from the beam, is adsorbed on both carbon steel surface and the $FeCO_3$ crystal, resulting in a $FeCO_3$-PAH hybrid layer. In the same manner, this adsorption mechanism is anticipated when PAH polymer is added at longer pre-corrosion periods (24, 34 and 44 h), but with a thicker $FeCO_3$-PAH hybrid layer since $FeCO_3$ had a longer time to be well-established.

This finding confirms the previous topographical observations in Figure 11, that the PAH polymer covers the carbon steel surface as well as $FeCO_3$ crystals. The thickness of $FeCO_3$ crystal layer in the absence of PAH polymer is 5 to 8 µm, whereas in the presence of PAH polymer is around 1 µm. The resulting $FeCO_3$-PAH hybrid layers are composed of $FeCO_3$ crystals with thickness between 450 to 1000 nm and the top adsorbed PAH polymer with thickness between 50 to 500 nm. Obtaining $FeCO_3$ fine crystals underneath PAH polymer layer potentially resulted from influence of PAH polymer on $FeCO_3$ nucleation/growth mechanism, as similar impact was found during nucleation and crystal growth of calcite [16]. $FeCO_3$ and $CaCO_3$ (calcite) are two isostructural minerals with rhombohedral crystal structure. Kinetically, $FeCO_3$ exhibits a nucleation/growth mechanism analogous to $CaCO_3$ (calcite) but orders of magnitude slower at comparable saturation [43].

It is worth mentioning that the adsorption of PAH polymer onto carbon steel surface and $FeCO_3$ crystal layer implies the segregation of steel surface from the corrosion media as a physical hydrophobic barrier leading to an instant reduction in corrosion process by time. This means the further transfer of Fe^{2+} ion from steel surface to the corrosion medium will be interrupted; hence the precipitation and nucleation ratio will be unbalanced leading to slower crystallisation of $FeCO_3$.

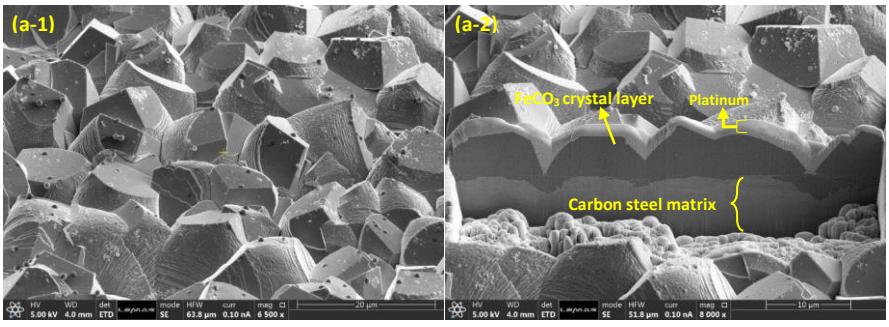

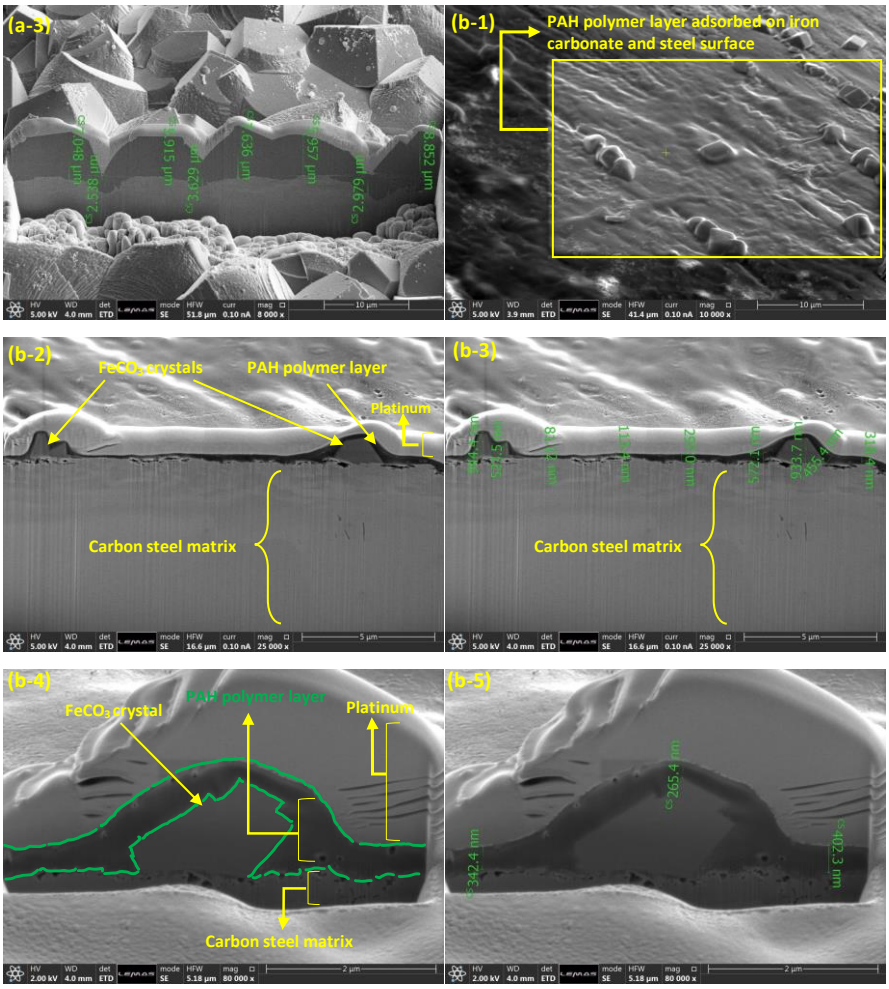

Figure 12. FIB cross-section micrographs of carbon steel exposed to electrolyte (pH=6.6, 60°C, 0.3 wt.% NaCl, pCO_2=0.8 bar) for two days. (a1-a3) is a blank while (b1-b3 and c1-c3) are in the presence of 100 ppm PAH polymer added after 2 h of pre-corrosion.

Figure 13 displays SEM micrograph of a specific area and its EDX mapping of the FIB cross-section for the test specimen exposed to 100 ppm PAH after 48 h with 2 h of pre-corrosion. From carbon mapping micrograph, it was noted that PAH polymer covers the carbon steel surface including the $FeCO_3$ crystals. Furthermore, the presence of $FeCO_3$ underneath PAH polymer is supported from mapping of iron and oxygen.

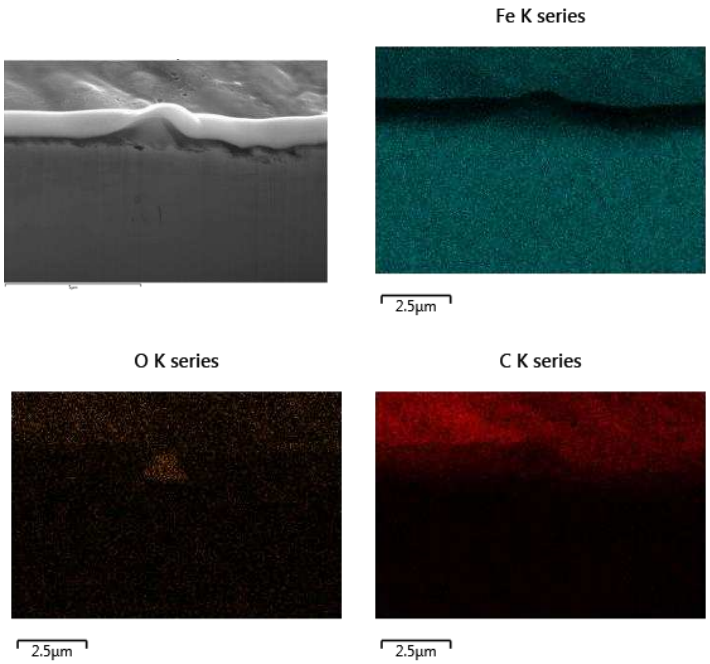

Figure 13. SEM (magnification size: 25K X) and EDX mapping micrographs of a selected area of FIB cross-section of carbon steel exposed to CO_2-saturated brine for 48 h containing 100 ppm of PAH polymer added after 2 h of pre-corrosion (pH=6.6, 60°C, 3.5 wt.% NaCl, pCO_3=0.8 bar).

Further detailed analysis of the FIB cross-section is provided in Figure 14, showing a single $FeCO_3$ crystal underneath the PAH polymer layer. This region was magnified and the resulting EDX line scans through the crystal and PAH polymer layer is shown in Figure 14. The carbon line scan indicates that the carbon content from the sides of the crystal is noticeably higher than within the crystal, whereas the scans associated with oxygen illustrate the opposite trend. This is attributed to the adsorption and presence of the PAH polymer over the $FeCO_3$ crystal. The iron line scan, however, is higher from outer side of $FeCO_3$ crystal which is due to the transparency and thickness of PAH polymer layer from the sides of the crystals resulting EDX beam collecting iron content from carbon steel surface. These observations are in alignment with SEM and FIB-SEM micrographs in **Figure 11** and **Figure 12** confirming that the portion of the steel surface is covered; so there is a reduction in anodic/cathodic activity, and consequently corrosion rate, as displayed in Figure 7.

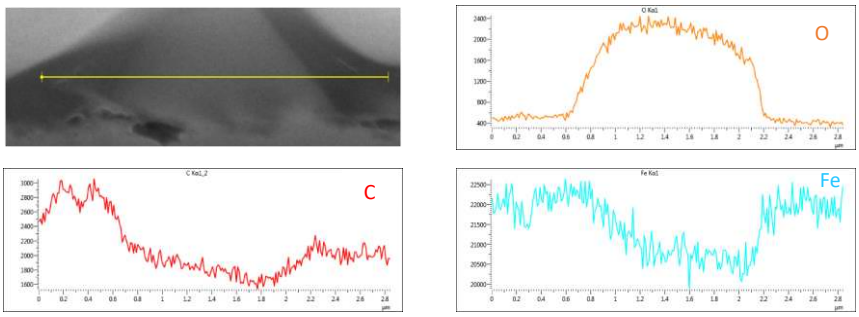

Figure 14. SEM and EDX line scan of a selected area of FIB cross-section of carbon steel exposed to CO_2-saturated brine for 48 h containing 100 ppm of PAH polymer added after 2 h of pre-corrosion. Test conditions are pH 6.6, 60°C, 3.5 wt.% NaCl, pCO_2=0.8 bar.

3.4. Localised corrosion

Due to the nature of the PAH polymer and its adsorption efficiency, it is anticipated that the addition of the polymer would improve mechanical properties of $FeCO_3$ layer as a $FeCO_3$-PAH hybrid layer, hence enhance the protective properties of the layer in terms of general and localised corrosion. Data in Table 7 depicts the extent of localised corrosion after 48 h of immersion testing with no PAH polymer, as well as with the PAH polymer addition at 24 and 34 h respectively. Consistent with previous work [45], the majority of the pitting in the investigated conditions occurs towards the latter stages of the experiment. The observations demonstrate that introducing PAH polymer resulted in the decrease of the total number of pits on the surface, as well as the pit depth. In comparison, a total of 126 micro-pits were found on steel surface with no PAH polymer after 48 h of exposure, whereas only 29 pits were found on the surface when the polymer was introduced in the system after 34 h of immersion testing. As expected, the PAH polymer exhibits a positive impact on localised corrosion retardation, with the pit depth decreasing from an average of 26 µm on sample with no polymer, to an average of 20 µm and 9 µm when the polymer was added at 24 and 34 h in turn.

Table 7. Localised corrosion data for the tests with no PAH polymer and presence of PAH polymer injected after 24 and 34 h. (pH 6.6, 60°C, 3.5 wt.% NaCl, pCO_3=0.8 bar and 48 h)

48 h exposure time	Average* Diameter, µm	Average* Depth, µm	Total pit count
No PAH polymer	25.06	26.24	126
PAH polymer at 24 h	25.23	19.61	11
PAH polymer at 34 h	32.10	9.05	29
	*Average of 10 deepest pits		

More interestingly, pits found on the surface in the presence of PAH polymer appear to have narrower diameters as it can be seen in Figure 15, with a decrease in depth after the injection of the polymer. It was discovered that introducing PAH polymer at a later stage of exposure time, i.e. when there is more $FeCO_3$ crystals on the metal surface, resulted in shallower pits, hence a less aggressive localised attack. This highlights the synergistic effect of PAH polymer on corrosion process to be able to interact with the corrosion product as well as steel surface. Such observations of PAH polymer are interesting, as numerous investigations with more 'conventional' CO_2 corrosion inhibitors report pre-corrosion and corrosion product formation having a detrimental influence on localised corrosion [12,13]. To optimise the PAH polymer dosage/pre-corrosion time with regard to localised corrosion and galvanic

interactions, the mechanism of localised corrosion retardation and galvanic corrosion should be explored further.

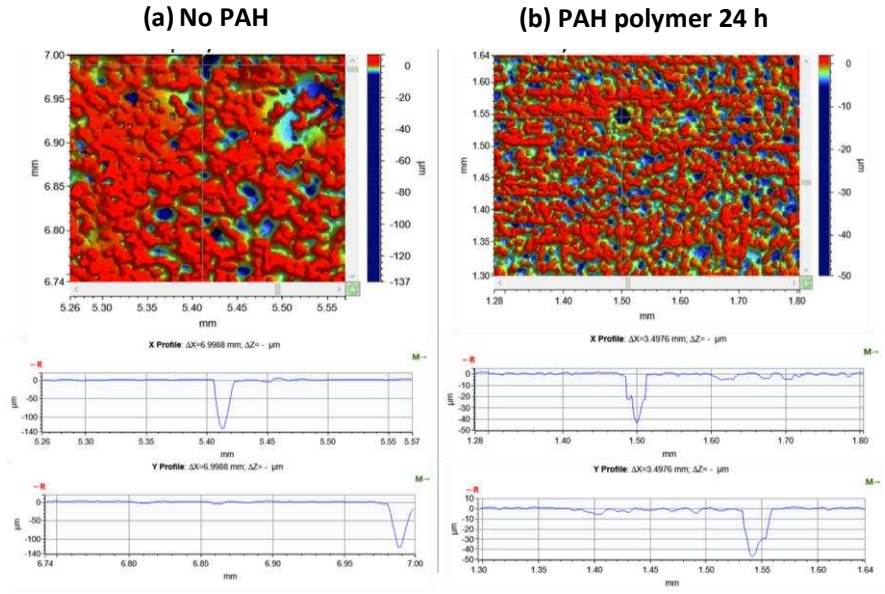

Figure 15. 2D pit morphologies after 48 h of immersion testing with no PAH polymer (a) and PAH polymer added after 24 h (b). (pH 6.6, 60°C, 3.5 wt.% NaCl and pCO_2=0.8 bar).

In the presence of pre-formed corrosion products, it is reported that the CO_2 corrosion inhibitors show poor general corrosion protection as well as promoting the localised corrosion [12,13]. To explore the general and localised corrosion protection of PAH polymer in the presence of $FeCO_3$ layer, the characterised corrosion rates extrapolated from LPR technique and localised corrosion (total pit count and average pit depth) at the end of 48 h exposure time for pure $FeCO_3$ layer and the hybrid $FeCO_3$ - PAH layer are plotted in Figure 16. Although the $FeCO_3$-PAH hybrid layer shows a slightly higher general corrosion rate compared with $FeCO_3$ layer alone, the PAH-$FeCO_3$ layer demonstrates a drastic decrease in total pit counts and average pit depths offering a more efficient layer for localised corrosion. This suggests that PAH polymer is adsorbed onto steel surface as well as $FeCO_3$ layer available on surface, which is consistent with obtained findings for surface analysis in Figure 11 and Figure 12. Hence, this data suggests that introducing PAH polymer at adequate stages of pre-corrosion to produce a hybrid structure not only results in co-operation with the $FeCO_3$ layer in reducing general corrosion but also retarding formation of new pits or growth of the pre-formed pits.

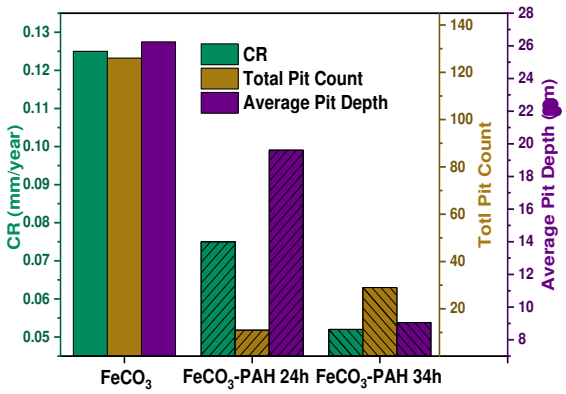

Figure 16. Comparison of corrosion rate values extrapolated from LPR investigation and localised corrosion (total pit count and average pit depth) after 48 h of immersion tests for $FeCO_3$ layer and hybrid layer, where PAH polymer was added at 24 and 34 h pre-corrosion. (pH 6.6, 60°C, 3.5 wt.% NaCl and pCO_3=0.8 bar).

3.5. Mechanical property characterisation

To compute the mechanical properties of studied $FeCO_3$ and $FeCO_3$ – PAH polymer layers, the nanoindentation and scratch test was employed. The layers were developed for 48 h exposure time in the absence and presence of PAH polymer added at 24, 34 and 44 h pre-corrosion.

3.5.1. Hardness and Young's modulus

Figure 17 shows the characterised hardness and Young's modulus for $FeCO_3$ and $FeCO_3$ – PAH polymer layers. Despite shorter exposure time in this study, the obtained hardness and Young's modulus of pure $FeCO_3$ layer in the absence of PAH polymer are comparable and consistent with our published mechanical properties of general corrosion products [26]. The hardness of all layers stays independent of administrating PAH polymer showing roughly constant values between 9 to 12 GPa. Conversely, the Young's modulus of developed hybrid $FeCO_3$ – PAH polymer layers is enhanced by a factor of 2 from values ranging between 100 and 250 GPa dependent on the pre-corrosion time of the polymer injection. This is due to the fact that the PAH polymer is interacting with a thicker $FeCO_3$ layer when added at later of the exposure time. Similar enhancement in shear stresses, discussed later, dependent on pre-corrosion time of PAH polymer injection are obtained. A higher Young's modulus is usually obtained after a reduction in the material's porosity and indicates higher mechanical flexibility. This mechanical enhancement of the $FeCO_3$ – PAH polymer modified corrosion layers can be attributed to the adsorption of organic PAH polymer as shown from morphological and FIB investigation in Figure 11 and Figure 12. Furthermore, the mechanical enhancement introduced by PAH is also in the same order of magnitude when various PAH polymer entities are blended with harder materials such as carbon nanotubes and graphene oxide [18,19,49]. A higher Young's modulus will help in resisting higher internal stresses and cohesive delamination that all corrosion layers are subjected to while developing thicker during the growth of the crystals. Additionally, improvement in the elasticity of the $FeCO_3$ layer is crucial since it provides the required tenacity and resistance to harsh environmental stresses such as erosive wear. Ultimately, the developed $FeCO_3$ – PAH hybrid layer is anticipated to be able to withstand various flow effects. The malleability and

elastic behaviour enhancement of $FeCO_3$-PAH hybrid layer is in a close agreement with removal shear stresses found during scratch test analysis discussed later. To explore the removal shear stresses and durability of the hybrid $FeCO_3$ – PAH hybrid layer comparable with $FeCO_3$ layer alone, scratch test was performed and outlined in the section 3.5.2 .

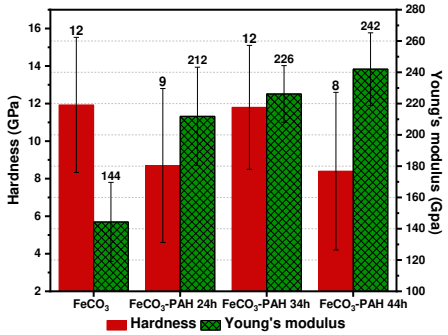

Figure 17. Investigated hardness and Young's modulus for $FeCO_3$ and $FeCO_3$ – PAH polymer layers, where PAH polymer introduced at 24, 34 and 44 h exposure time (pH=6.6, 60°C, 3.5 wt.% NaCl, pCO_3=0.8 bar, 48 h).

3.5.2. Scratch test analysis

Prior to scratch testing, the carbon steel specimens were corroded in CO_2-saturated brine (48 h, pH 6.6, 60°C, 3.5 wt.% NaCl and pCO_2=0.8 bar) to develop pure $FeCO_3$ and $FeCO_3$-PAH hybrid layers, where the polymer was added at different pre-corrosion times (24, 34 and 44 h). On these specimens, a progressive load scratch was performed from 1 to 50 N, as per parameters listed previously in Table 3, to determine the critical load required to remove the layers. After each scratch test, the removal stages were determined using optical microscopy and SEM analysis. The microscopical images of these progressive scratches are shown in Figure 18.

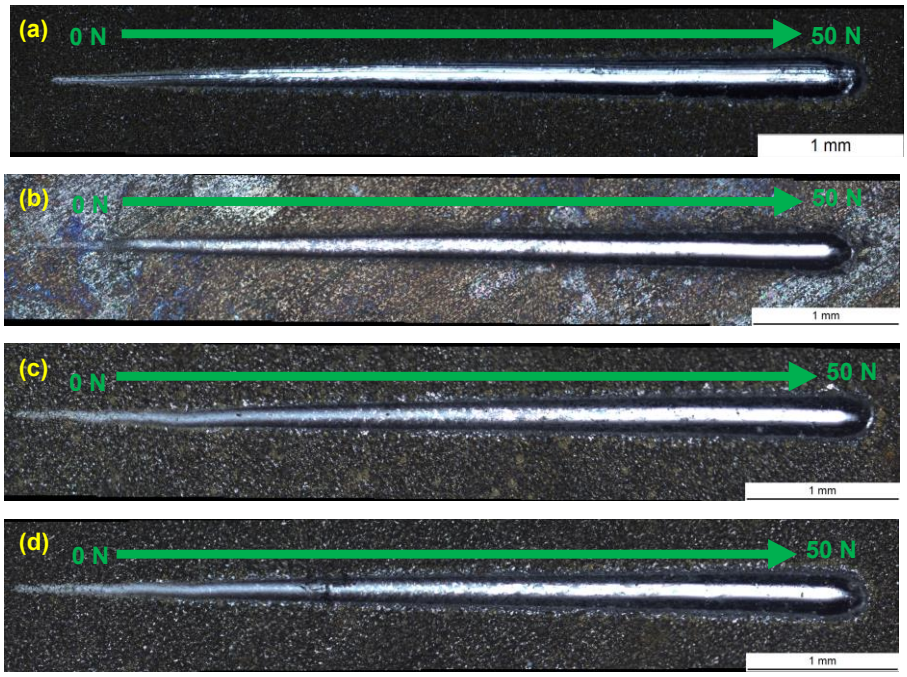

Figure 18. Optical microscope images of progressive scratch test from 1 to 50 N on carbon steel surfaces with protective layers: (a) pure $FeCO_3$ from uninhibited tests. (b, c and d) are $FeCO_3$-PAH hybrid layers where the 100 ppm of PAH polymer was introduced at 24, 34 and 44 h of pre-corrosion, respectively.

From the microscope images, it was noticed that the coexistence of PAH polymer with $FeCO_3$ as a hybrid layer on the surface required significantly higher forces in comparison with pure $FeCO_3$, to eliminate the layers on the surface of carbon steel. To charcterise the scratch tracks and determine the precise radius of minimum damage, partial removal and full delamination on pure $FeCO_3$ and $FeCO_3$-PAH hybrid layers, the morphology of surfaces was analysed further with SEM and EDX, as shown in Figure 19.

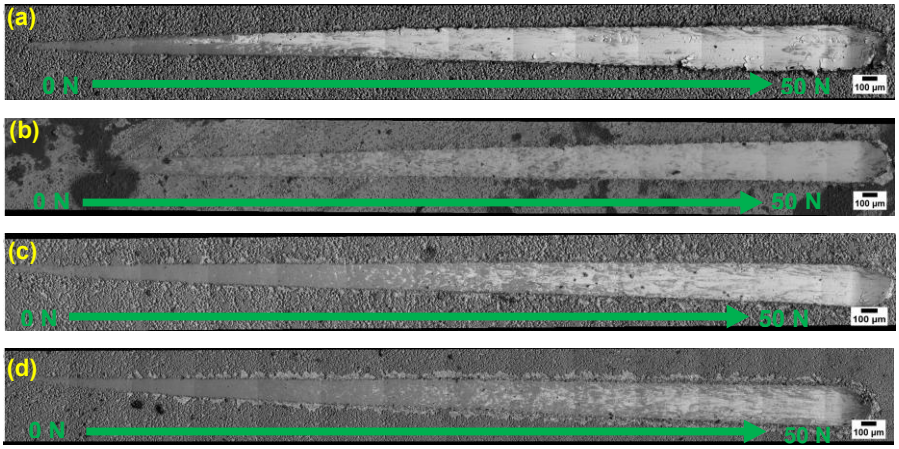

Figure 19. SEM images of progressive scratch test from 1 to 50 N on carbon steel surfaces with protective layers: (a) pure $FeCO_3$ from uninhibited tests. (b, c and d) are $FeCO_3$-PAH hybrid layers where the 100 ppm of PAH polymer was introduced at 24, 34 and 44 h of pre-corrosion, respectively.

From SEM topographical images, the bare surface of carbon steel becomes visible in a shorter distance in the scratch test for pure $FeCO_3$, (Figure 19(a)), while in the tracks of $FeCO_3$-PAH hybrid layers, the bare surface of the steel appears at longer distances, (Figure 19(b, c and d)).

To understand how the difference between noticeable damage, buckling failure and total delamination was determined, a schematic illustration is provided in Figure 20(a1-a3). The SEM analysis, in combination with scratch test data analysis (discussed in the methodology section and shown in Table 8), indicated that the minimum force to cause noticeable damage to pure $FeCO_3$ layer was around 7.7 N, while for $FeCO_3$-PAH hybrid layers was approximately 11 N. As the applied load progressively increases, more damage is generated to all layers, until the buckling or adhesive failure of pure $FeCO_3$ layer achieved at a load of 15 N. However, twice that load was required to obtain buckling failure in the $FeCO_3$-PAH hybrid layers. Furthermore, the detachment load of the pure $FeCO_3$ layer was half of that required to detach the $FeCO_3$-PAH hybrid layers from carbon steel surface. All the related micrographs and loaded forces are presented in Figure 20 and Table 8, respectively. The higher force of detachment for $FeCO_3$-PAH hybrid layers in comparison with pure $FeCO_3$ layer indicates that PAH polymer enhances the adherence force of $FeCO_3$ on carbon steel. This is consistent with previous studies which showed that PAH polymer improved adhesion property in mechanomutable materials [50] and enhanced tensile strength and Young's modulus in graphene oxide composite [18].

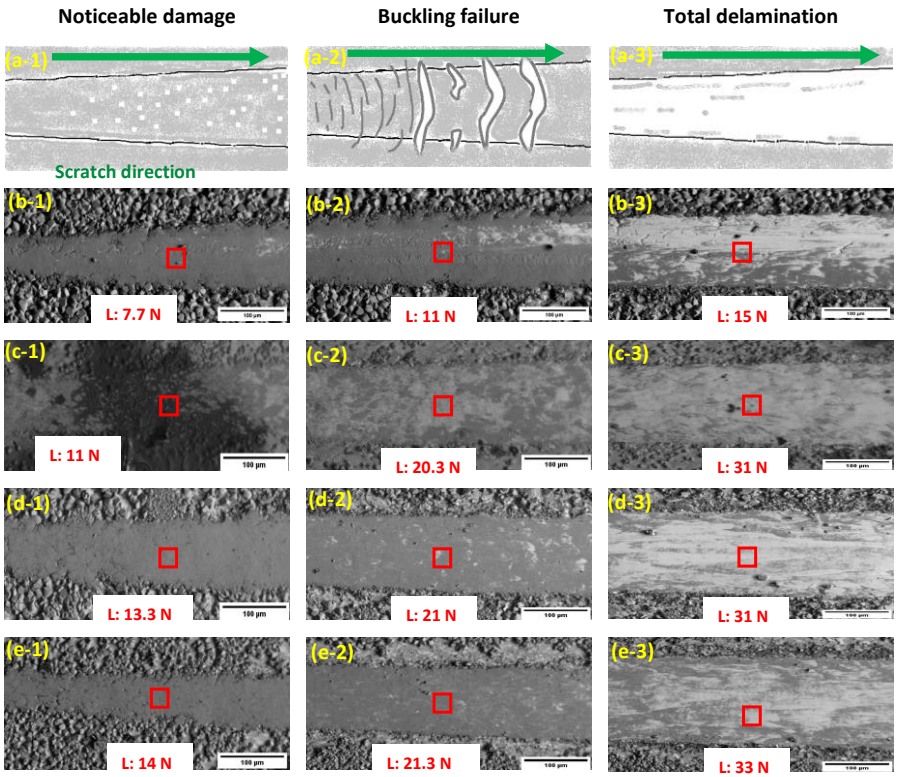

Figure 20. SEM micrographs (magnigfication size: 100X) of scratch test specimens indicating noticeable damage, buckling failure and total delamination. (a) schematic/illustration [51,52], (b) $FeCO_3$ layer and (c, d, e) hybrid PAH-$FeCO_3$ layers, where 100 ppm of PAH polymer was added after 24, 34 and 44 h of pre-corrosion, respectively.

Table 8. Determined loads of noticeable damage, partial removal and full delamination for $FeCO_3$ and $FeCO_3$-PAH hybrid layers.

Surface / Parameter	$FeCO_3$	Hybrid layer 24 h pre-corrosion	Hybrid layer 34 h pre-corrosion	Hybrid layer 44 h pre-corrosion
Minimum force to create a noticeable damage (cohesive failure)	7.7 ± 0.75 N	11 ± 0.8 N	13.3 ± 0.47 N	14 ± 0.34 N
Load to partially remove the layer (adhesive failure critical load)	11 ± 0.51 N	20.3 ± 0.63 N	21 ± 0.38 N	21.3 ± 0.91 N
Load to totally remove the layer (full delamination)	15 ± 0.77 N	31 ± 0.9 N	31 ± 0.53 N	33 ± 0.57 N

Another interesting finding was that the adsorbed PAH polymer content was higher in some areas of surface than others. These high content PAH polymer areas resulted in the polymer exhibiting higher resistance against the scratch load, as shown in Figure 21. From magnified SEM micrographs and EDX elemental mapping in Figure 21, it is clear that the PAH polymer is still adhered and stretched within the tracks of the scratch. The elemental maps characterise the dominant area of PAH polymer inside and outside of scratch tracks. From these results it can be concluded that the resistive PAH polymer was smeared onto surface due to the load but protects the $FeCO_3$ crystals underneath from buckling and removal. This adhesion character of PAH polymer is reported to improve the tensile strength of lignocellulosic fibrous networks and graphene oxide composite [18,49].

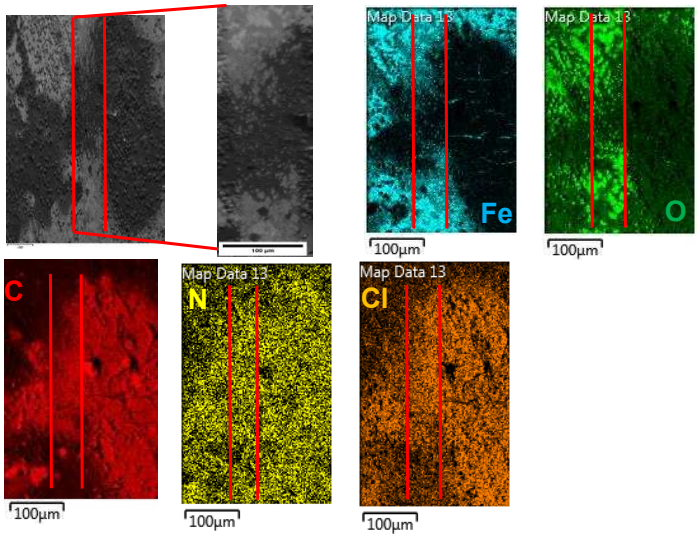

Figure 21. SEM (magnigfication size: 500X) and EDX mapping within the track of the scratch test for a $FeCO_3$-PAH hybrid layer on carbon steel.

3.5.3. Shear stress for cohesive failure, adhesive failure and full removal

The determined shear stresses for cohesive failure, adhesive failure and full delamination of $FeCO_3$ and $FeCO_3$-PAH hybrid layers are calculated, as explained in section 2.6.2, and presented in Figure 22.

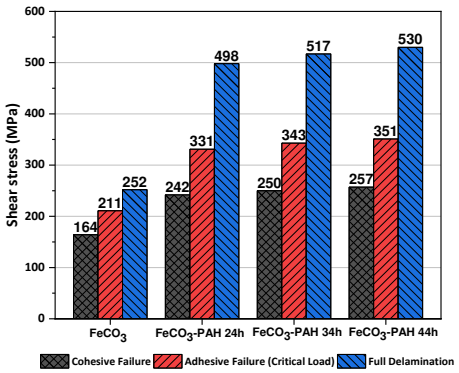

Figure 22. Summary of calculated failure shear stresses, using the Oliver and Pharr model, of $FeCO_3$ and $FeCO_3$-PAH hybrid layers generated through the addition of 100 ppm PAH to the brine solution after 24, 34 and 44 h of pre-corrosion.

From the shear stress analysis of Figure 22, the $FeCO_3$-PAH hybrid layers withstood higher shear stresses compared to those for the pure $FeCO_3$ layer. The minimal damage (cohesive failure) of $FeCO_3$ layer was achieved at 164 ± 5 MPa, whereas the shear stress to cause minimal damage in hybrid films was 242 ± 15 MPa. The shear stress to achieve adhesive failure point of $FeCO_3$-PAH hybrid layers was 100 MPa higher than that of pure $FeCO_3$ at the same point. Ultimately, the $FeCO_3$-PAH hybrid layer requires double the shear stress compared to that of the pure $FeCO_3$ layer for full delamination, which is in consistent with Young's modulus enhancement extent found for $FeCO_3$-PAH hybrid layer in section 3.5.1. These results suggest that the presence of PAH polymer produces a hybrid film which is more adherent than the original $FeCO_3$ corrosion product layer, and that PAH is able to significantly enhance the mechanical properties of an existing $FeCO_3$ layer.

In multiphase flow, the maximum determined wall shear stress of pipeline is of the order of 100 Pa when investigated at ambient condition, while the highest practical wall shear stress of could be expected to be of the order of 1 kPa [53]. The shear stress required for removal of an organic corrosion inhibitor film on carbon steel has been widely investigated in the last two decades. Gulbrandsen and Grana, for instance, utilised a jet impingement setup and found that the CO_2 corrosion inhibitor performance was independent of flow velocity up to 20 m/s with a calculated wall shear stress up to 1400 Pa [54]. In another study, the shear stress required to remove a tall oil fatty acid imidazolium inhibitor from the steel surface was determined by AFM to be 50-100 MPa [42], whereas the shear stress needed to scratch off the imidazoline film (4 nm) from carbon steel was estimated to be in the range of 50 MPa [55]. In comparison with the aforementioned conventional organic inhibitors, PAH polymer holds a higher removal shear stress of 150 MPa, which is at least three orders of magnitude above the maximum shear stress obtained by realistic fluid flow in pipelines (1 kPa) even under the most severe hydrodynamic conditions. These observations for the PAH polymer are promising, but the effect of flow on layer removal and reformation should be experimentally validated.

It should be stressed that the observed critical loads and shear stresses of pure $FeCO_3$ in this study are lower than what were listed in literature [29,56,57]. The factors behind this disagreement may vary. One strong reason can be the different corrosion condition parameters of which $FeCO_3$ was developed, such as substrate composition, pH, temperature, duration of experiment, pCO_2 and salinity. Another conceivable impact might be the method of formation of $FeCO_3$. In previous work,

$FeCO_3$ layer was deposited using higher initial levels of saturation in the bulk solution, while the current study commences experiments with no Fe^{2+} ions added to the solution during the investigation duration. For instance, Prieto et al. [29], supplied extra ferrous ion (Fe^{2+}) initially into the bulk solution and the experiment was performed at 80°C, pH 8 and for three days. In comparison with their results, the $FeCO_3$ in the current study is developed in lower temperature, pH, and evolution time (Table 2). Consequently, these parameters and bulk chemical conditions play a key role in the adhesion strength and density of the $FeCO_3$ crystal layer as a corrosion product, and clearly require further investigation.

4. Conclusions

In this study, poly(allylamine hydrochloride) is applied as a multi-functional form of treatment to reduce the degradation of carbon steel in CO_2-containing aqueous environments. This is achieved through the *in-situ* fabrication of a $FeCO_3$-PAH hybrid layer on the carbon steel surface via the introduction of PAH polymer part way through the formation of $FeCO_3$ on the steel surface. From this study the following conclusions can be made:

- The $FeCO_3$-PAH hybrid layer acts as mixed-type corrosion inhibitor and has been shown to provide adequate corrosion rate protection with corrosion rate values close to 0.1 mm/yr.
- The hybrid corrosion layer was shown to drastically reduce the localised corrosion attack as depicted by the tenfold decrease in the number of pits but also the reduction in the pit depth.
- The newly formed hybrid layer demonstrates better mechanical properties, mainly higher Young's modulus as shown by both nanoindentation and scratch test which implicates a higher resistance to internal stresses and cohesive failures. It is anticipated that such mechanical property enhancements will extend the lifetime of the protective $FeCO_3$-PAH hybrid layer.

Acknowledgments

The authors would like to acknowledge the funding and technical support from Danish Hydrocarbon Research and Technology Centre (DHRTC) which made this research possible. We would like to give special thanks to Prof Rajan Ambat, Kitt Anita Ravnkilde, Dr Nicolas Bovet and Yanina Dragomilova Ivanova of Mechanical Engineering Department, Technical University of Denmark for their valuable comments, feedback and support during this work. Many thanks to the technical support from the Institute of Functional Surfaces at Leeds.

5. References

[1] S. Papavinasam, Corrosion Control in the Oil and Gas Industry, 2013. https://doi.org/10.1016/C2011-0-04629-X.

[2] T.E. Perez, Corrosion in the Oil and Gas Industry: An Increasing Challenge for Materials, JOM. 65 (2013) 1033–1042. https://doi.org/10.1007/s11837-013-0675-3.

[3] F. Backus, E. Harvey, M. Gunn, Evaluation and application of calcite scale inhibitor in an offshore pH stabilised MEG system—an Australian first, APPEA J. 55 (2015) 247. https://doi.org/10.1071/aj14019.

[4] J. Kvarekval, A. Dugstad, Corrosion mitigation with ph stabilisation in slightly sour gas/condensate pipelines, in: NACE - Int. Corros. Conf. Ser., 2006.

[5] R. Barker, D. Burkle, T. Charpentier, H. Thompson, A. Neville, A review of iron carbonate (FeCO3) formation in the oil and gas industry, Corros. Sci. 142 (2018) 312–341. https://doi.org/10.1016/j.corsci.2018.07.021.

[6] X. Wen, P. Bai, B. Luo, S. Zheng, C. Chen, Review of recent progress in the study of corrosion products of steels in a hydrogen sulphide environment, Corros. Sci. (2018). https://doi.org/10.1016/j.corsci.2018.05.002.

[7] P. Jin, S. Nesic, Mechanism of magnetite formation in high temperature naphthenic acid corrosion by crude oil fractions, Corros. Sci. 115 (2017) 93–105. https://doi.org/10.1016/j.corsci.2016.11.021.

[8] M. Alizadeh, S. Bordbar, The influence of microstructure on the protective properties of the corrosion product layer generated on the welded API X70 steel in chloride solution, Corros. Sci. 70 (2013) 170–179. https://doi.org/10.1016/j.corsci.2013.01.026.

[9] M. Di Bonaventura, B. Brown, S. Nešić, M. Singer, Effect of flow and steel microstructure on the formation of iron carbonate, Corrosion. 75 (2019) 1183–1193. https://doi.org/10.5006/3118.

[10] Y. Yang, Removal Mechanisms of Protective Iron Carbonate Layer in Flowing Solutions, Ohio University, 2012. http://rave.ohiolink.edu/etdc/view?acc_num=ohiou1339731278 (accessed June 20, 2020).

[11] Y. Yang, B. Brown, S. Nesic, Study of protective iron carbonate layer dissolution in a CO2 corrosion environment, in: NACE - Int. Corros. Conf. Ser., 2013.

[12] A. Shamsa, R. Barker, Y. Hua, E. Barmatov, T.L. Hughes, A. Neville, Performance evaluation of an imidazoline corrosion inhibitor in a CO2-saturated environment with emphasis on localised corrosion, Corros. Sci. (2020). https://doi.org/10.1016/j.corsci.2020.108916.

[13] H. Zhang, X. Pang, M. Zhou, C. Liu, L. Wei, K. Gao, The behavior of pre-corrosion effect on the performance of imidazoline-based inhibitor in 3 wt.% NaCl solution saturated with CO 2, Appl. Surf. Sci. 356 (2015) 63–72. https://doi.org/10.1016/j.apsusc.2015.08.003.

[14] C. Aparicio, M.P. Ginebra, Biomineralization and biomaterials: fundamentals and applications, Woodhead Publishing, 2015.

[15] P.M. Dove, J.J. De Yoreo, S. Weiner, Biomineralization, Walter de Gruyter GmbH & Co KG, 2018.

[16] B. Cantaert, Y.-Y. Kim, H. Ludwig, F. Nudelman, N.A.J.M. Sommerdijk, F.C. Meldrum, Think Positive: Phase Separation Enables a Positively Charged Additive to Induce Dramatic Changes in Calcium Carbonate Morphology, Adv. Funct. Mater. 22 (2012) 907–915. https://doi.org/10.1002/adfm.201102385.

[17] A.S. Schenk, B. Cantaert, Y.-Y. Kim, Y. Li, E.S. Read, M. Semsarilar, S.P. Armes, F.C. Meldrum, Systematic Study of the Effects of Polyamines on Calcium Carbonate Precipitation, Chem. Mater. 26 (2014) 2703–2711. https://doi.org/10.1021/cm500523w.

[18] A. Satti, P. Larpent, Y. Gun'Ko, Improvement of mechanical properties of graphene oxide/poly(allylamine) composites by chemical crosslinking, Carbon N. Y. 48 (2010) 3376–3381. https://doi.org/10.1016/j.carbon.2010.05.030.

[19] A. Satti, A. Perret, J.E. McCarthy, Y.K. Gun'Ko, Covalent crosslinking of single-walled carbon

nanotubes with poly(allylamine) to produce mechanically robust composites, J. Mater. Chem. 20 (2010) 7941–7943. https://doi.org/10.1039/c0jm01515f.
[20] M.S. Sarwar, Q. Huang, A. Ghaffar, M.A. Abid, M.S. Zafar, Z. Khurshid, M. Latif, A Smart Drug Delivery System Based on Biodegradable Chitosan/Poly(allylamine hydrochloride) Blend Films, Pharmaceutics. 12 (2020) 131. https://doi.org/10.3390/pharmaceutics12020131.
[21] B.D.B. Tiu, R.C. Advincula, Polymeric corrosion inhibitors for the oil and gas industry: Design principles and mechanism, React. Funct. Polym. 95 (2015) 25–45. https://doi.org/10.1016/j.reactfunctpolym.2015.08.006.
[22] E. McCafferty, Introduction to corrosion science, Springer Science & Business Media, 2010. https://doi.org/10.1007/978-1-4419-0455-3.
[23] Z. Ahmad, Principles of Corrosion Engineering and Corrosion Control, 2006. https://doi.org/10.1016/B978-0-7506-5924-6.X5000-4.
[24] N. V Chukanov, A.D. Chervonnyi, Infrared spectroscopy of minerals and related compounds, Springer, 2016.
[25] G. ASTM, G 1-03, Standard Practice for Preparing, Cleaning and Evaluating Corrosion Test Specimens, in: Am. Soc. Test. Mater., 2003.
[26] W. Taleb, F. Pessu, C. Wang, T. Charpentier, R. Barker, A. Neville, Siderite micro-modification for enhanced corrosion protection, Npj Mater. Degrad. 1 (2017) 13. https://doi.org/10.1038/s41529-017-0014-1.
[27] W.C. Oliver, G.M. Pharr, An improved technique for determining hardness and elastic modulus using load and displacement sensing indentation experiments, J. Mater. Res. 7 (1992) 1564–1583. https://doi.org/10.1557/jmr.1992.1564.
[28] G171-03(2017), Standard Test Method for Scratch Hardness of Materials Using a Diamond Stylus, in: ASTM B. Stand., 2003. https://doi.org/10.1520/G0171-03R09E02.2.
[29] C. Prieto, E. Anyanwu, D. Young, M. Singer, Mechanical characterization and adherence of iron carbonate on an X65 steel, in: NACE - Int. Corros. Conf. Ser., 2019.
[30] S.J. Bull, E.G. Berasetegui, An overview of the potential of quantitative coating adhesion measurement by scratch testing, Tribol. Int. 39 (2006) 99–114. https://doi.org/10.1016/j.triboint.2005.04.013.
[31] E. Hart, Corrosion inhibitors: Principles, mechanisms and applications, in: Corros. Inhib. Princ. Mech. Appl., InTech, 2016: pp. 1–161. https://doi.org/10.5772/57255.
[32] A. Reisch, P. Tirado, E. Roger, F. Boulmedais, D. Collin, J.C. Voegel, B. Frisch, P. Schaaf, J.B. Schlenoff, Compact saloplastic poly(acrylic acid)/poly(allylamine) complexes: Kinetic control over composition, microstructure, and mechanical properties, Adv. Funct. Mater. 23 (2013) 673–682. https://doi.org/10.1002/adfm.201201413.
[33] M. Javidi, R. Chamanfar, S. Bekhrad, Investigation on the efficiency of corrosion inhibitor in CO2 corrosion of carbon steel in the presence of iron carbonate scale, J. Nat. Gas Sci. Eng. 61 (2019) 197–205. https://doi.org/10.1016/j.jngse.2018.11.017.
[34] K. Kousar, M.S. Walczak, T. Ljungdahl, A. Wetzel, H. Oskarsson, P. Restuccia, E.A. Ahmad, N.M. Harrison, R. Lindsay, Corrosion inhibition of carbon steel in hydrochloric acid: Elucidating the performance of an imidazoline-based surfactant, Corros. Sci. 180 (2021) 109195. https://doi.org/10.1016/j.corsci.2020.109195.
[35] M. Yadav, D. Behera, U. Sharma, Nontoxic corrosion inhibitors for N80 steel in hydrochloric acid, Arab. J. Chem. 9 (2016) S1487–S1495. https://doi.org/10.1016/j.arabjc.2012.03.011.
[36] R. Lindsay, S.B. Lyon, Introduction to control of corrosion by environmental modification, in: Shreir's Corros., Elsevier, 2010: pp. 2891–2899. https://doi.org/10.1016/B978-044452787-5.00159-1.
[37] P.E. Alvarez, M.V. Fiori-Bimbi, A. Neske, S.A. Brandán, C.A. Gervasi, Rollinia occidentalis extract as green corrosion inhibitor for carbon steel in HCl solution, J. Ind. Eng. Chem. 58 (2018) 92–99. https://doi.org/10.1016/j.jiec.2017.09.012.
[38] F. Farelas, M. Galicia, B. Brown, S. Nesic, H. Castaneda, Evolution of dissolution processes at

the interface of carbon steel corroding in a CO2 environment studied by EIS, Corros. Sci. 52 (2010) 509–517. https://doi.org/10.1016/j.corsci.2009.10.007.
[39] M. Gao, X. Pang, K. Gao, The growth mechanism of CO2 corrosion product films, Corros. Sci. 53 (2011) 557–568. https://doi.org/10.1016/j.corsci.2010.09.060.
[40] V. Zucolotto, M. Ferreira, Ḿarcia R. Cordeiro, C.J.L. Constantino, D.T. Balogh, A.R. Zanatta, W.C. Moreira, O.N. Oliveira, Unusual interactions binding iron tetrasulfonated phthalocyanine and poly(allylamine hydrochloride) in layer-by-layer films, J. Phys. Chem. B. 107 (2003) 3733–3737. https://doi.org/10.1021/jp027573d.
[41] R.J.G. Rubira, P.H.B. Aoki, C.J.L. Constantino, P. Alessio, Supramolecular architectures of iron phthalocyanine Langmuir-Blodgett films: The role played by the solution solvents, Appl. Surf. Sci. 416 (2017) 482–491. https://doi.org/10.1016/j.apsusc.2017.04.155.
[42] Y. Xiong, B. Brown, B. Kinsella, S. Nešić, A. Pailleret, Atomic force microscopy study of the adsorption of surfactant corrosion inhibitor films, Corrosion. (2014). https://doi.org/10.5006/0915.
[43] C.Z. Jiang, N.J. Tosca, Growth kinetics of siderite at 298.15 K and 1 bar, Geochim. Cosmochim. Acta. 274 (2020) 97–117. https://doi.org/10.1016/j.gca.2020.01.047.
[44] O. Devos, C. Gabrielli, M. Tlili, B. Tribollet, Nucleation-Growth Process of Scale Electrodeposition, J. Electrochem. Soc. 150 (2003) C494. https://doi.org/10.1149/1.1580825.
[45] F. Pessu, R. Barker, A. Neville, The influence of pH on localized corrosion behavior of X65 carbon steel in CO2-saturated brines, Corrosion. 71 (2015) 1452–1466. https://doi.org/10.5006/1770.
[46] H. Matthiesen, L.R. Hilbert, D.J. Gregory, Siderite as a Corrosion Product on Archaeological Iron from a Waterlogged Environment, Stud. Conserv. 48 (2003) 183–194. https://doi.org/10.1179/sic.2003.48.3.183.
[47] A.M. Stingel, C. Calabrese, P.B. Petersen, Strong intermolecular vibrational coupling through cyclic hydrogen-bonded structures revealed by ultrafast continuum mid-IR spectroscopy., J. Phys. Chem. B. 117 (2013) 15714–9. https://doi.org/10.1021/jp406441r.
[48] K. Sakota, Y. Kageura, H. Sekiya, Cooperativity of hydrogen-bonded networks in 7-azaindole(CH3OH)n (n=2,3) clusters evidenced by IR-UV ion-dip spectroscopy and natural bond orbital analysis, J. Chem. Phys. 129 (2008) 054303. https://doi.org/10.1063/1.2961031.
[49] A. Marais, L. Wågberg, The use of polymeric amines to enhance the mechanical properties of lignocellulosic fibrous networks, Cellulose. 19 (2012) 1437–1447. https://doi.org/10.1007/s10570-012-9712-6.
[50] S.W. Cranford, C. Ortiz, M.J. Buehler, Mechanomutable properties of a PAA/PAH polyelectrolyte complex: Rate dependence and ionization effects on tunable adhesion strength, Soft Matter. 6 (2010) 4175–4188. https://doi.org/10.1039/c0sm00095g.
[51] S.J. Bull, Failure Mode Maps in the Thin Film Scratch Adhesion Test, Tribol. Int. 30 (1997) 491–498.
[52] C1624 (latest revision), Standard test method for adhesion strength and mechanical failure modes of ceramic coatings by quantitative single point scratch testing, n.d.
[53] W. Li, B.F.M. Pots, B. Brown, K.E. Kee, S. Nesic, A direct measurement of wall shear stress in multiphase flow—Is it an important parameter in CO 2 corrosion of carbon steel pipelines?, Corros. Sci. 110 (2016) 35–45. https://doi.org/10.1016/j.corsci.2016.04.008.
[54] E. Gulbrandsen, A. Grana˚, Testing of Carbon Dioxide Corrosion Inhibitor Performance at High Flow Velocities in Jet Impingement Geometry. Effects of Mass Transfer and Flow Forces, CORROSION. 63 (2007) 1009–1020. https://doi.org/10.5006/1.3278316.
[55] S. Nesic, Effects of multiphase flow on internal CO 2 corrosion of mild steel pipelines, Energy and Fuels. 26 (2012) 4098–4111. https://doi.org/10.1021/ef3002795.
[56] W. Li, Y. Xiong, B. Brown, K.E. Kee, S. Nesic, Measurement of wall shear stress in multiphase flow and its effects on protective FeCO3 corrosion product layer removal, NACE Corros. Conf. 2015. (2018).

[57] Y. Yang, B. Brown, S. Nešić, M. Elena Gennaro, B. Molinas, Mechanical strength and removal of a protective iron carbonate layer formed on mild steel in CO2 corrosion, in: NACE - Int. Corros. Conf. Ser., 2010.